Dwarfs in the Milky Way halo outer rim: first infall or backsplash satellites?

Matías Blaña [ID],[1,2]★ Andreas Burkert,[1,2,3] Michael Fellhauer [ID],[4] Marc Schartmann[1,2,3] and Christian Alig[2]

[1]*Max-Planck-Institut für extraterrestrische Physik, Gießenbachstraße 1, D-85748 Garching bei München, Germany*
[2]*Universitäts-Sternwarte, Fakultät für Physik, Ludwig-Maximilians-Universität München, Scheinerstraße 1, D-81679 München, Germany*
[3]*Excellence Cluster ORIGINS, Boltzmannstr 2, D-85748 Garching bei München, Germany*
[4]*Departamento de Astronomía, Universidad de Concepción, Avenida Esteban Iturra s/n, Casilla 160-C, 4030000 Concepción, Chile*

ABSTRACT

Leo T is a gas-rich dwarf located at 414 kpc (1.4$R_{\rm vir}$) distance from the Milky Way (MW) and it is currently assumed to be on its first approach. Here, we present an analysis of orbits calculated backwards in time for the dwarf with our new code DELOREAN, exploring a range of systematic uncertainties, e.g. MW virial mass and accretion, M31 potential, and cosmic expansion. We discover that orbits with tangential velocities in the Galactic standard-of-rest frame lower than $|\vec{u}_{\rm t}^{\rm GSR}| \leq 63^{+47}_{-39}$ km s^{-1} result in backsplash solutions, i.e. orbits that entered and left the MW dark matter halo in the past, and that velocities above $|\vec{u}_{\rm t}^{\rm GSR}| \geq 21^{+33}_{-21}$ km s^{-1} result in wide-orbit backsplash solutions with a minimum pericentre range of $D_{\rm min} \geq 38^{+26}_{-16}$ kpc, which would allow this satellite to survive gas stripping and tidal disruption. Moreover, new proper motion estimates overlap with our orbital solution regions. We applied our method to other distant MW satellites, finding a range of gas stripped backsplash solutions for the gasless Cetus and Eridanus II, providing a possible explanation for their lack of cold gas, while only first infall solutions are found for the H I-rich Phoenix I. We also find that the cosmic expansion can delay their first pericentre passage when compared to the non-expanding scenario. This study explores the provenance of these distant dwarfs and provides constraints on the environmental and internal processes that shaped their evolution and current properties.

Key words: methods: numerical – galaxies: individual: Leo T – Local Group – galaxies: dwarfs.

1 INTRODUCTION

The transient H I gas-rich dwarf galaxy Leo T, discovered by Irwin et al. (2007), is currently in the outskirts of the Milky Way (MW), at $D_\odot = 409^{+29}_{-27}$ kpc from the Sun (Clementini et al. 2012) with a Galactic standard-of-rest (GSR) line-of-sight (LOS) stellar velocity of $v_{\rm los,\star}^{\rm GSR} = -65.9 \pm 2.0$ km s^{-1} [Simon & Geha 2007; recalculated for the MW Galactocentric coordinates (GCs) adopted in this work]. Adams & Oosterloo (2018) (hereafter AO18) performed deep H I observations of Leo T that show with exquisite detail its gas density and kinematic properties (see Fig. 1), which present features that suggest an ongoing interaction with the MW gaseous halo through ram-pressure stripping. This makes Leo T not only an ideal laboratory to study the formation and evolution of dwarfs (Read, Agertz & Collins 2016), but also a probe to study the properties of the hot halo of the MW, which is the environment where these dwarfs live (Grcevich & Putman 2009; Gatto et al. 2013; Belokurov et al. 2017).

An observed property of dwarfs in the MW and M31 is that, excluding the Magellanic Cloud satellites, most satellites located within the MW's virial radius ($R_{\rm vir} = 282 \pm 30$ kpc for a virial mass of $M_{\rm vir} = 1.3 \pm 0.3 \times 10^{12}$ M$_\odot$; Bland-Hawthorn & Gerhard 2016, hereafter BG16) show very little or no neutral gas, while most of the dwarfs located beyond the host's virial radius show gas-to-stellar-light ratios larger than 1 (Blitz & Robishaw 2000; McConnachie 2012; Spekkens et al. 2014), with some interesting exceptions such as Cetus I and Tucana. The gas loss in dwarfs would be a natural result of environmental interactions with the host galaxy through ram-pressure stripping, tidal disruption, and ultraviolet (UV) background gas evaporation (Mori & Burkert 2000; Sawala, Scannapieco & White 2012; Simpson et al. 2018; Buck et al. 2019; Hausammann, Revaz & Jablonka 2019), as well as internal effects, such as stellar feedback (Read et al. 2016).

An important prediction from cosmological galaxy simulations is the existence of two types of populations of satellites located near the virial radius of a host galaxy at redshift zero: field satellites that are currently falling for the first time into the halo of the host, and another population of satellites that are currently on their second infall, called 'backsplash' or 'fly-by' satellites, which are found in a Local Group (LG) context (Teyssier, Johnston & Kuhlen 2012; Garrison-Kimmel et al. 2017) and in galaxy groups and clusters (Gill et al. 2005; Lotz et al. 2019; Haggar et al. 2020; Diemer 2020). The backsplash population can represent an important fraction between 30 and 50 per cent of the satellites located between one and two times the virial radius at redshift zero (Rodriguez Wimberly et al. 2018; Simpson et al. 2018; Buck et al. 2019). Among the backsplash population, they find gas-rich satellites, as well as gas-poor satellites, which would depend on internal processes and also on the amount of gas stripping that the satellite endured during its orbital path. And, more importantly, Buck et al. (2019) show that the backsplash population and the first infall population can have similar gas fractions; however, their baryon-to-dark matter
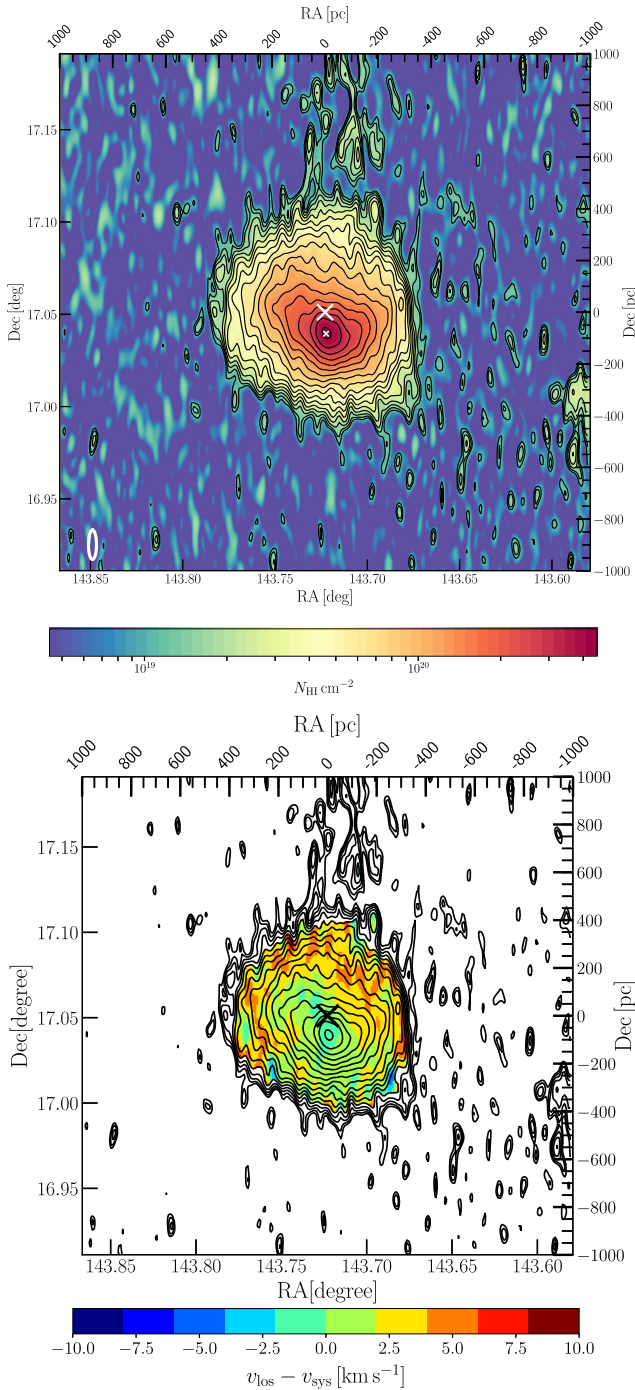
★ E-mail: mblana@mpe.mpg.de

Figure 1. H I observations from AO18 performed with the Westerbork Synthesis Radio Telescope. The optical or stellar centre is at the origin of the axes in pc units and is marked in both the panels by a large cross. Top panel: column density map and iso-contours between 10^{19} and 4.2×10^{20} cm^{-2} logarithmically spaced every 0.1 dex. The small cross marks the H I density peak location. The beaming size is marked with the white ellipse (bottom left). Bottom panel: column density iso-contours and H I LOS velocity map where we subtracted the stellar systemic velocity $v_{los,\star}^{\odot}$.

fractions can be quite different, as the former could have lost up to 50 per cent of their initial dark matter masses due to tidal stripping (see also van den Bosch et al. 2018). This makes determining the orbital history of the satellites extremely important to understand the main drivers of their evolution (Hausammann et al. 2019; Tonnesen

2019), and to use them as probes of the gaseous halo of the MW. Furthermore, from cosmological MW-type simulations presented in Teyssier et al. (2012), Simpson et al. (2018), and Buck et al. (2019) are predicted the likelihoods of MW satellites being a backsplash system depending on their distances and LOS velocities with respect to the host galaxy, finding, for example, for Leo T a likelihood of 50–70 per cent. Interesting as well is that Leo T is located near the first caustic or splashback radius of MW-type cosmological simulated galaxies (Deason et al. 2020), (see also Diemer et al 2017a,b). However, cosmological galaxy simulations provide only statistical comparisons of properties and evolution histories of dwarfs and their hosts, while here we use observations of dwarfs to calculate different orbits, exploring the parameter space of several uncertainties, such as the MW virial mass and more.

In this paper, we investigate the possible origin of Leo T by studying backsplash orbital solutions as well as the first infall solutions. For this, we develop a new method and a software called DELOREAN to calculate orbits backwards in time considering a range of scenarios. We also apply our new code to study the orbits of the dwarfs Cetus, Phoenix I, and Eridanus II. The paper is ordered as follows: In Section 2, we detail the main properties and observations of Leo T. In Section 3, we explain our new software to set up and calculate the orbits, and the method to analyse them. The results are presented and discussed in Section 4, and concluded in Section 5.

2 LEO T OBSERVATIONS AND PROPERTIES

We present the main properties of Leo T in Table 1. Leo T is a gas-rich dwarf located at $1.45 R_{vir}$ distance from the Galactic Centre, located at $D_{\odot} = 409$ kpc (Clementini et al. 2012). de Jong et al. (2008) estimate that Leo T possesses an old stellar population with a V-band luminosity of $L_V = 8.9 \times 10^4$ L$_{\odot}$ within five half-light radii and also a younger population of stars (between $\sim$200 Myr and 1 Gyr in age) with $L_V = 5.1 \times 10^4$ L$_{\odot}$. They estimate a combined luminosity of $L_V = 1.4 \times 10^5$ L$_{\odot}$, with the younger stars contributing approximately 10 per cent of the total stellar mass. Weisz et al. (2012) find a stellar mass of 10^5 M$_{\odot}$ within one half-light radius. The younger population is evidence that Leo T can still form stars, although there is no strong evidence of molecular gas so far (AO18). This is consistent with star formation history studies that show a small and fluctuating star formation rate with an average of $\sim$$10^{-5}$ M$_{\odot}$ yr^{-1}, with two peaks of high rates at 1–2 and 7–9 Gyr ago (Clementini et al. 2012; Weisz et al. 2012).

The systemic GSR stellar velocity of Leo T is $v_{los,\star}^{\odot} = -65.9 \pm 2.0$ km s^{-1}. The stellar proper motion $\mu_{\alpha*}$, μ_{δ} of this dwarf is unknown. Taking a zero tangential velocity in the GSR frame ($\vec{u}_t^{GSR} = 0$ km s^{-1}) transforms into the proper motion values of $\mu_{\alpha*}^{\circ} = -0.0150$ mas yr^{-1} and $\mu_{\delta}^{\circ} = -0.1153$ mas yr^{-1}, which is just the proper motion in the direction of Leo T due to the motion of the Sun relative to the Galactic Centre. The stellar and gas kinematics indicate that this dwarf is dark matter dominated, as determined by LOS velocity dispersions between 7 and 8 km s^{-1} (Table 1), implying a dynamical mass within 400 pc of 10^6–10^7 M$_{\odot}$ (Simon & Geha 2007; Ryan-Weber et al. 2008; Faerman, Sternberg & McKee 2013; Adams & Oosterloo 2018; Patra 2018), with a circular velocity V_c between 7 and 14 km s^{-1}, similar to other dwarfs (McConnachie 2012).

Leo T has a relatively massive H I reservoir (Ryan-Weber et al. 2008; Grcevich & Putman 2009; Faerman et al. 2013; AO18) with an estimated H I mass of 3.8×10^5 M$_{\odot}$, which is 5 per cent lower than the original value reported in AO18 (4.1×10^5 M$_{\odot}$), because we have re-scaled the observations to the latest distance estimate of 409 kpc, instead of the 420 kpc used in the original publication.

Table 1. Main properties of Leo T.

RA	$09^{\rm h}34^{\rm m}53^{\rm s}.4$ [a]
Dec.	$+17^{\rm o}03'05''$ [a]
$D_\odot$	409^{+29}_{-27} kpc [b]
$D^{\rm GC}$	414^{+29}_{-27} kpc [c]
$v_{\rm los,\star}^\odot$	38.1 ± 2.0 km s^{-1} [d]
$v_{\rm los,\star}^{\rm GSR}$	-65.9 ± 2.0 km s^{-1} [e, c, d]
$\mu_{\alpha^*}^\circ\,(\vec{u}^{\rm GSR}=0\,{\rm km\,s^{-1}})$	-0.0150 mas yr^{-1} [e, c]
$\mu_\delta^\circ\,(\vec{u}_{\rm t}^{\rm GSR}=0\,{\rm km\,s^{-1}})$	-0.1153 mas yr^{-1} [e, c]
$X^{\rm GC}, Y^{\rm GC}, Z^{\rm GC}$	$(-250, -169, 283)$ kpc [c]
$V_X^{\rm GC}, V_Y^{\rm GC}, V_Z^{\rm GC}$	$(39.1, 27.2, -45.5)$ km s^{-1} [e, c]
$M_{\rm V}$	-8.0 mag [f]
$L_{\rm V}$	$1.41 \pm \times 10^5\,{\rm L}_\odot$ [f]
$R_{\rm h}^{\rm V}$	73 ± 8 arcsec (145 ± 15 pc) [f]
$M_{\rm half}^\star$	$1.05^{+0.27}_{-0.23} \times 10^5\,{\rm M}_\odot$ [g]
$\sigma_{\rm los,\star}$	7.5 ± 1.6 km s^{-1} [d]
$M_{\rm half}^{\rm dyn}$	$7.6 \pm 3.3 \times 10^6\,{\rm M}_\odot$ [c, d]
$M^{\rm HI}$	$3.8 \pm 0.4 \times 10^5\,{\rm M}_\odot$ [h, c]
$R_{\rm HI}$	106 ± 10 arcsec (210 ± 20 pc) [c]
$M_{\rm Pl}^{\rm HI}$	$4.1 \pm 0.4 \times 10^5\,{\rm M}_\odot$ [c]
$\Sigma_{\rm Pl}^{\rm HI}$	$3.48 \pm 0.33 \times 10^6\,{\rm M}_\odot\,{\rm kpc}^{-2}$ [c]
$N_{\rm Pl}^{\rm HI}$	$4.34 \pm 0.45 \times 10^{20}\,{\rm cm}^{-2}$ [c]
$\rho_{\rm Pl}^{\rm HI}$	$1.35 \pm 0.13 \times 10^7\,{\rm M}_\odot\,{\rm kpc}^{-3}$ [c]
$n_{\rm Pl}^{\rm HI}$	0.54 ± 0.05 cm^{-3} [c]
$M^{\rm gas}$	$5.2 \pm 0.5 \times 10^5\,{\rm M}_\odot$ [h, c]
$M_{\rm Pl}^{\rm gas}$	$5.5 \pm 0.5 \times 10^5\,{\rm M}_\odot$ [c]
$\Sigma_{\rm Pl}^{\rm gas}$	$4.64 \pm 0.45 \times 10^6\,{\rm M}_\odot\,{\rm kpc}^{-2}$ [c]
$\rho_{\rm Pl}^{\rm gas}$	$1.79 \pm 0.17 \times 10^7\,{\rm M}_\odot\,{\rm kpc}^{-3}$ [c]
$R_{\rm Pl}^{\rm gas}$	97.81 ± 0.03 arcsec (193.94 ± 0.06 pc) [c]
$r_{\rm 3D\text{-}half,\,Pl}^{\rm gas}$	130.41 ± 0.04 arcsec (258.59 ± 0.08 pc) [c]
$v_{\rm los,gas}^\odot$	39.6 ± 0.1 km s^{-1} [h]
$v_{\rm los,gas}^{\rm GSR}$	-64.4 ± 0.1 km s^{-1} [h, c]

Variables and symbols are explained in the main text. [a]Irwin et al. (2007). [b]Clementini et al. (2012). [c]calculated in this publication or re-calculated from estimations in the literature that are re-scaled to a heliocentric distance of Leo T of 409 kpc, using a conversion from heliocentric to GC or GSR coordinates with the solar values presented in Section 3.1. [d]Simon & Geha (2007). [e]Values when the GSR tangential velocity is assumed to be zero ($|\vec{u}_{\rm t}^{\rm GSR}| = 0$ km s^{-1}). [f]de Jong et al. (2008). [g]Weisz et al. (2012). [h]Adams & Oosterloo (2018).

Taking a helium-to-hydrogen gas mass ratio of 0.33, we obtain a gas mass of $M^{\rm gas} = 5.2 \pm 0.5 \times 10^5\,{\rm M}_\odot$, which does not include the ionized gas that could be surrounding the dwarf. This results in an H I-mass-to-stellar-light ratio of $M_{\rm HI}/L_{\rm V} = 2.7\,{\rm M}_\odot\,{\rm L}_\odot^{-1}$ and a gas-mass-to-stellar-light ratio of $M_{\rm gas}/L_{\rm V} = 3.6\,{\rm M}_\odot\,{\rm L}_\odot^{-1}$. Assuming a stellar-mass-to-light ratio of $2\,{\rm M}_\odot\,{\rm L}_\odot^{-1}$ would give us a gas-mass-to-stellar-mass ratio of $M_{\rm HI}/M_\star \sim 1.3$.

To estimate the central density and surface density, we calculate the surface density profile fitting the H I map of AO18 with ELLIPSE (Jedrzejewski 1987), shown in Fig. 2, and fitted a Plummer function to obtain the central gas density and the Plummer radius of the gas (Table 1), which we use in Section 3.3 to calculate the thermal pressure. We also interpolate the H I profile of the observations to calculate $R_{\rm HI}$, the radius where $\Sigma^{\rm HI}(R_{\rm HI}) = 1\,{\rm M}_\odot\,{\rm pc}^{-2} = 1.248 \times 10^{20}\,{\rm cm}^{-2}$ (Broeils & Rhee 1997; Wang et al. 2016), with errors estimated from the 10 per cent uncertainties in the H I mass.

The H I distribution in Leo T also reveals a very interesting morphology. The observations of AO18 in Fig. 1, performed with the Westerbork Synthesis Radio Telescope (WSRT), reveal exquisite
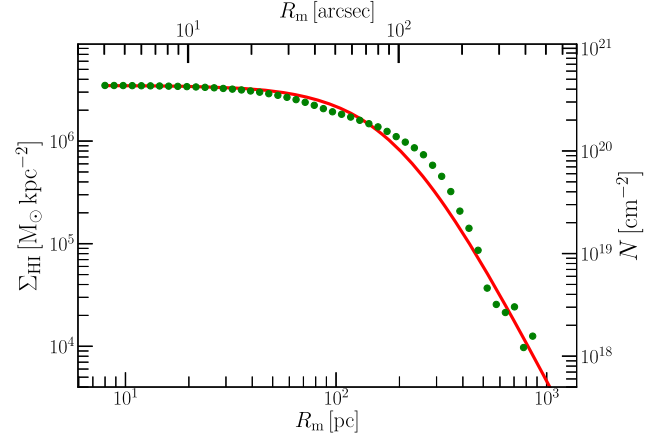

Figure 2. Azimuthally averaged H I surface mass profile as a function of the ellipse major axis of ellipses fitted to the H I observations (AO18) (green dots) and the Plummer fit (red curve), with the fit parameters shown in Table 1.

details in the H I density and kinematics. We list some features reported by AO18 below:

(i) The central gas iso-contours are systematically more compressed towards the southern side, with a compressed edge to the west as well, showing a trapezoidal flattened shape. This could be produced by a bow shock as the dwarf moves through the MW hot halo, producing the observed flattening that would be then perpendicular to the direction of motion of the dwarf. Under this assumption, we measure the orientation of this flattening by fitting ellipses and finding the position angle of the minor axis of the ellipse at PA$_{\rm flat} = -21^\circ$, which we can use later to constrain the orientation of the orbits on the sky.

(ii) The H I velocity map shows a gradient from south to north of about ~ 16 km s^{-1} kpc^{-1}, reaching up to $+5$ km s^{-1} from the systemic velocity in the northern part, which would be then lagging behind. This is comparable to the circular velocity value $V_{\rm c}(0.25\,{\rm kpc}) \approx 13$ km s^{-1}.

(iii) The high H I surface density peak is shifted in projection 83 pc (42 arcsec) south from the optical centre, at RA $= 143.722^\circ$ and Dec $= 17.0394^\circ$. Ryan-Weber et al. (2008) report a similar offset of 40 arcsec with the Giant Meterwave Radio Telescope and also previous WSRT measurements. Furthermore, the deeper WSRT observations of AO18 report that the global H I distribution is indeed centred near the stellar centre and that only the inner region is shifted south. A similar offset has been observed in the dwarf Phoenix I as well. If this offset is related to the interaction between this dwarf and the MW corona, we could use its orientation to constrain its motion on the sky. We find that the line connecting the optical centre with the H I density peak is at a position angle of PA$_{\rm offset} = 3^\circ$.

(iv) Finally, there is an unreported faint tail of H I material collected in clumps of different sizes extending to the north from the optical centre, at approximately PA$_{\rm tail} = -10^\circ \pm 10^\circ$. While the tail substructure is at the limit of detection, considering the additional H I features that have a similar alignment in PA builds a convincing scenario of a hydrodynamical interaction between Leo T and the MW corona, where the origin of the tail could be the dwarf's gas being stripped and that is trailing the dwarf. We will further explore this with full hydrodynamical simulations in a future publication.

We decide to use the stellar (optical) centre and the stellar systemic LOS velocity of Leo T ($v_{\rm los,\star}^\odot$) as our orbital initial conditions, given that the kinematics of the gas shows perturbations, such as

an H I velocity gradient and the offset between the stars and the gas. Furthermore, given that Leo T is dark matter dominated, the stellar kinematics should remain almost unaffected by the gravitational force of the perturbed gas density arising from the ram pressure. Moreover, we note that the H I systemic velocity is only 1.5 km s^{-1} slower than the stellar one.

3 METHOD

In this paper, we want to find constraints for the current tangential velocity of Leo T by calculating different orbits backwards in time and estimating for what values of the tangential velocity the orbit would have experienced a gas stripping from the MW weak enough to allow the satellite to keep its gas, and for which velocities the gas would have been completely removed. We also estimate for what values of the tangential velocity we can find orbits that would have entered the dark halo of the MW in the past. In the following section, we explain our new orbital integrator code, and the set-up to explore the space of free parameters such as tangential velocities with different directions and magnitudes, and the scenarios that explore different gravitational potentials, dynamical friction effects, and effects due to the cosmic expansion.

3.1 Orbit integrator code

To perform the orbital exploration forward or backwards in time for the dwarfs or objects, we developed an orbit integrator code in PYTHON called Dwarfs and clustErs orbitaL integratOR codE and ANalysis or more simply DELOREAN,[1] which has three modules.

The first module converts the Heliocentric coordinates of the dwarfs (or object) to GSR coordinates and Cartesian GCs using ASTROPY routines (The Astropy Collaboration 2013, 2018), where we use a solar distance to the Galactic Centre of $R_0 = 8.2$ kpc, a solar height above the galactic disc of $z_0 = 25$ pc, and a GC solar motion of $\vec{v}_\odot^{GC} = (11 \pm 1, 248 \pm 3, 7.3 \pm 0.5)$ km s^{-1} (BG16). The code has the option to explore heliocentric proper motion values pre-defined by the user, or it can construct the vector $\vec{u}_t^{GSR}$, which is the velocity vector in the GSR frame at the current position of the object that is tangential to the LOS velocity, following a prescription explained in Appendix A. We explore different directions of $\vec{u}_t^{GSR}$ and magnitudes $|\vec{u}_t^{GSR}|$. For Leo T, we explore 36 different directions of the tangential velocity $\vec{u}_t^{GSR}$ (every $\Delta PA = 10°$) and we add two more directions in the grid (see Section 4.1.4). We sample the magnitude ($|\vec{u}_t^{GSR}|$) from 0 to 10 km s^{-1} every 0.5 km s^{-1}, then from 12 to 180 km s^{-1} every 2 km s^{-1}, from 180 to 300 km s^{-1} every 10 km s^{-1}, and finally from 300 to 350 km s^{-1} every 50 km s^{-1}, exploring then in total a grid with 4218 values of $\vec{u}_t^{GSR}$.

In the second module, the code uses a leap-frog scheme to integrate the orbits backward or forward in time, with an option for variable time-step (Δt), where we use this to calculate the orbits 12 Gyr backwards in time. For efficiency, we use as default in our set-up a time-step of $\Delta t = 1$ Myr, testing the accuracy of the orbit calculation with $\Delta t = 0.1$ Myr and with a variable time-step scheme. It has options to use a drift-kick-drift or kick-drift-kick scheme. The orbits are calculated as test particles moving within a set-up of a combination of gravitational potentials that are available in the code. Each set-up or scenario of potentials is defined here as a case, which is specified in Section 3.2. For the cases that simultaneously include the potentials of the MW and M31, the code pre-computes M31 and

[1]Soon available at http://matiasblana.github.io.

Table 2. Set-up of main parameters for all cases.

MW	$M_{vir}(\times 10^{12}\,M_\odot)$	R_{vir} (kpc)	c
cases	1.3	288	8.6
subcases a	1.0	264	8.4
subcases b	1.6	308	8.8
cases	MW potential	M31?	Cosmo?
1	static	no	no
2	evolving	no	no
3	static	yes	no
4	evolving	yes	no
5	static	no	no
cos3	static	yes	yes
cos4	evolving	yes	yes

Notes. By static or evolving MW potential, we mean that the MW parameters M_{vir}, R_{vir}, and c are constant in time (static) or evolve with redshift. M31?: informs if the orbits of M31 and the MW were pre-computed and their orbits and potentials included in the orbital calculation of the satellite. Cosmo?: informs if the orbits were calculated using the cosmological equations of motion (Section 3.1).

MW orbiting each other in a two-body scheme, to then compute the orbits of the dwarfs as test particles moving in the also moving and joint potentials of MW and M31 (see case 3 in Section 3.2). Furthermore, our code DELOREAN can also integrate orbits backward or forward in time in an expanding Universe (or contracting if it is time reversed), which is further explained in Appendix A.

In the third module, the code has routines to calculate dynamical and hydrodynamical quantities analytically after the orbit calculations are finished. We determine the tidal radius as a function of time as

$$R^{tidal}(D, t) = D(t) \left(\frac{m_{Sat}}{3 M_{host}(D, t)} \right)^{1/3}, \qquad (1)$$

where m_{Sat} is the satellite's virial mass, $D(t)$ is the distance between the host galaxy (MW) and the satellite as a function of time during the orbit (comoving coordinates in case a cosmological scheme is chosen), and $M_{host}(D, t)$ is the mass of the host (MW) enclosed within $D(t)$. This module also calculates the analytical ram-pressure-stripping force and other hydrodynamical quantities measured for each orbit, which are explained in Section 3.3.

3.2 Set-ups for the gravitational potentials

In order to quantify the orbital variations due to uncertainties in the gravitational potential, we consider in total 13 cases or set-ups for our modelling. These cases consider extreme scenarios, including, for example, a constant virial mass that implies an instantaneous mass accretion at high redshift, and other scenarios with a redshift-dependent MW mass accretion rate according to extended Press–Schechter models. We included more variations by changing the final MW virial mass and concentration, the influence of the Andromeda galaxy, the dynamical friction, and the cosmic expansion. We summarize the main properties of these cases in Table 2. The details of each case are the following:

(i) Cases 1, 1a, and 1b: Here we consider a static MW potential with a Navarro-Frenk-White (NFW) dark matter halo with a virial mass of $M_{vir} = 1.3 \pm 0.3 \times 10^{12}\,M_\odot$ (BG16). We note that this virial mass estimation includes the mass contribution from all the satellites living within the halo. We use a constant virial radius of $R_{vir} = 288$ kpc estimated from M_{vir} for redshift zero ($z = 0$), calculated as in Mo, van den Bosch & White (2010) with the virial radius in physical

units defined as

$$r_{\mathrm{vir}} = \left(\frac{M_{\mathrm{vir}}(z)}{4/3 \, \pi \, \rho_{\mathrm{crit}}(z) \, \Omega_{\mathrm{m}}(z) \, \Delta_{\mathrm{vir}}(z)} \right)^{1/3}, \qquad (2)$$

where the cosmological parameters ρ_{crit}, Ω_{m}, and Δ_{vir} are, respectively, the critical density, the matter-to-critical density ratio, and the spherical collapse overdensity criterion $\Delta_{\mathrm{vir}} \approx (8\pi^2 + 82\epsilon - 39\epsilon^2)(\epsilon + 1)^{-1}$ with $\epsilon = \Omega_{\mathrm{m}} - 1$. The comoving virial radius is then $R_{\mathrm{vir}} = r_{\mathrm{vir}}/a(z)$. The concentration parameter is $c = 8.6$, which is obtained from the halo concentration–mass relation from Correa et al. (2015a). We include a Plummer potential for the inner spheroid component with a mass of $M_{\mathrm{s}} = 5 \times 10^9 \, \mathrm{M}_\odot$ (Bovy 2015) and a scale length of 0.3 kpc, and a Miyamoto–Nagai disc potential with a mass of $M_{\mathrm{disc}} = 5.5 \times 10^{10} \, \mathrm{M}_\odot$ that encompasses the stellar and gaseous disc masses (BG16), with a scale length of 2.5 kpc and a scale height of 0.3 kpc. In cases 1a and 1b (and in all the following cases with subcases a and b), we explore the uncertainties in M_{vir}, c, and R_{vir}, using $1.0 \times 10^{12} \, \mathrm{M}_\odot$, 8.8, and 264 kpc for subcases (a), and $1.6 \times 10^{12} \, \mathrm{M}_\odot$, 8.4, and 308 kpc for subcases (b).

(ii) Cases 2, 2a, and 2b: We explore a time-varying MW potential, where the halo is accreting mass as a function of redshift. For this, we use the software COMMAH that provides solutions to the semianalytical extended Press–Schechter formalism (Press & Schechter 1974; Bond et al. 1991) and the halo mass accretion history models fitted to cosmological simulations to estimate evolution of the halo properties as a function of redshift (z) (Correa et al. 2015a, b, c). We use the values of the set-up of case 1 for the current ($z = 0$) virial mass, radius, and concentration parameter to calculate the variation of these parameters as a function of redshift (z): $c(z)$, $M_{\mathrm{vir}}(z)$, and $R_{\mathrm{vir}}(z)$, as shown in Fig. A1. For the disc and spheroid components, we assume that their masses (M_{comp}) change with redshift (or lookback time) in the same proportion as the halo, i.e. $M_{\mathrm{comp}}(z) = M_{\mathrm{comp}}(0) \, M_{\mathrm{halo}}(z)/M_{\mathrm{halo}}(0)$.

(iii) Cases 3, 3a, and 3b: We explore the influence of the gravitational potential of Andromeda (M31) on the orbits of the satellite, as it orbits the MW. For this, we set up the MW as in case 1 and we set a NFW potential for M31 and pre-compute the orbits 12 Gyr backwards in time for MW and M31 orbiting each other. The virial mass of M31 is usually assumed to be larger than that of the MW; however, the low abundance of tracers at large radii of up to 500 kpc results in substantial uncertainties in the measurement of M_{vir}, with values in the literature of $M_{\mathrm{vir}} = 1.6 \pm 0.6 \times 10^{12} \, \mathrm{M}_\odot$ (Watkins, Evans & An 2010) or $M_{\mathrm{vir}} = (0.8{-}1.1) \times 10^{12} \, \mathrm{M}_\odot$ (Tamm et al. 2012). Here we use the upper value of Tamm et al. (2012), choosing $M_{\mathrm{vir}} = 1.1 \times 10^{12} \, \mathrm{M}_\odot$ and $R_{\mathrm{vir}} = 266.3$ kpc, which still remains within other estimates in the literature. We show in Section 4.1 that, while the potential of M31 has an impact on the MW satellite orbits, the virial mass of the MW is what more strongly dominates the orbital properties at first order. For the pre-computation of the orbits of the MW and M31, we use constant virial masses and radii, as M31 and the MW are far enough that both systems are attracted by the whole regions that later assemble each in the MW and M31. For the orbit of M31, we use the heliocentric LOS velocity of $v_{\mathrm{los}}^{\mathrm{M31},\odot} = -301 \pm 1$ km s^{-1} (Courteau & van den Bergh 1999) and the proper motions $\mu_{\alpha*}^{\mathrm{M31}} = 64 \pm 18 \times 10^{-3}$ mas yr^{-1} and $\mu_{\delta}^{\mathrm{M31}} = -57 \pm 15 \times 10^{-3}$ mas yr^{-1} (van der Marel et al. 2018). Then, we calculate the orbits of the satellite in the moving potentials of the MW and M31. We also test MW–M31 orbits with different tangential velocities for M31 (including zero tangential velocity), finding small differences in the orbits of Leo T.

(iv) Case 4, 4a, and 4b: We compute the orbits of the satellite in the MW–M31 moving potentials, but where the MW potential is

also changing with redshift due to the mass accretion as case 2. As with the previous case, for the pre-computation of the orbits of the MW and M31, we use a constant MW virial mass, as M31 is far enough that it is attracted by the whole region that later assembles the MW. Case 4 corresponds to our fiducial scenario, as this includes the effects of the most relevant quantities.

(v) Case 5: We set up a scenario as case 1, but where we include a deceleration term due to the dynamical friction, using the Chandrasekhar approximation (equation 8.6 in Binney & Tremaine 2008). We note that this term accelerates an object if the orbit is calculated backwards in time. Case 5c: As in case 5, but we set up a scenario with an accreting MW as in case 2. We also test the friction effect using full *N*-body simulations (see Section 4.3).

(vi) Cases cos3 and cos4: We explore the effects of the cosmic expansion in the calculation of the orbits of the dwarfs for cases 3 and 4 (see Section 4.2).

While currently we do not include major merger events in the modelling, we expect that our wide range of MW mass models and their time dependence can reflect the impact of these merger events. The satellite orbits that we explore here go to large distances, spending most of their time near their apocentres, at around $1 R_{\mathrm{vir}}$ and $2.6 R_{\mathrm{vir}}$, and therefore their orbits are mostly affected by the MW total mass. Accretion events such as Sagittarius (Fellhauer et al. 2006; Niederste-Ostholt et al. 2010; Ruiz-Lara et al. 2020) and Sausage/Enceladus (Belokurov et al. 2018; Deason et al. 2018; Haywood et al. 2018; Helmi et al. 2018) have progenitors with estimated masses between 0.1 and 10 per cent of the MW virial mass, and we explored variations of radial mass profiles larger than this. For example, for the extreme cases, case 1b has a static MW mass model with a constant dynamical mass within 20 kpc of $M(R < 20 \, \mathrm{kpc}) = 15.3 \times 10^{10} \, \mathrm{M}_\odot$, while the mass accreting MW case 2a has a lower mass of $7.0 \times 10^{10} \, \mathrm{M}_\odot$ at $T = -8$ Gyr, at the time of the closest pericentre passages of radial satellite orbits (see 4.1), and even lower at -10 Gyr with $4.7 \times 10^{10} \, \mathrm{M}_\odot$.

Despite the large mass variations in the centre, we find that the main orbital constraints do not have extreme changes depending on the case (4.1). Therefore, we expect that merger events in the MW centre will vary the main orbital constraints within our range of result. There is, however, a probability that these satellites might have had a close interaction with a merger event at early times, but it would be unlikely given that these long distance orbits have fast pericentre passages, spending there only ~ 400 Myr. Moreover, despite all of this, even if such a close interaction actually occurred, it would have likely transpired in the central region of the MW, and given the advantage in our method where the orbits of the satellites are calculated backwards in time, they would still be correct until this event in the past.

3.3 Gas stripping estimation

We estimate the ram pressure experienced by the satellite for each orbit using the analytical estimators from Mori & Burkert (2000). They find that a gas-rich satellite galaxy that moves through the medium of its host galaxy will lose its gas if the ram pressure (P_{R}) that the satellite experiences by the environment of the host becomes larger than the thermal pressure that allows the dwarf to retain its gas (P_{T}); i.e. if the satellite is ram-pressure stripped by the host, we will have $P_{\mathrm{R}}/P_{\mathrm{T}} > 1$. The ram pressure is then given by

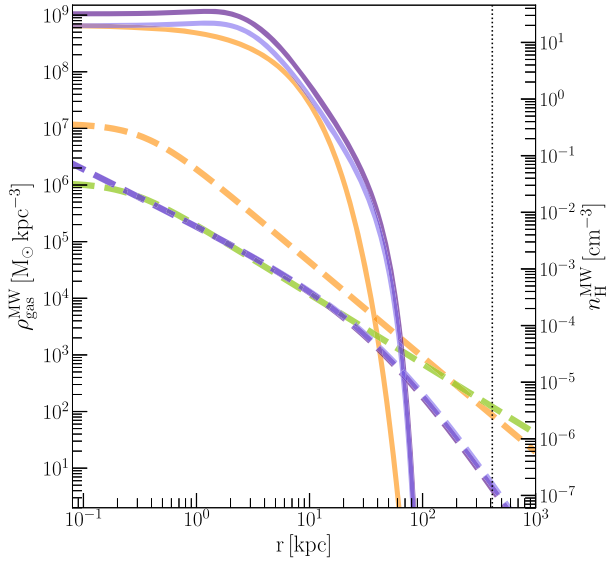$$P_{\mathrm{R}} = \rho_{\mathrm{gas}}^{\mathrm{medium}} V^2, \qquad (3)$$

Figure 3. Analytical MW gas mass density and hydrogen number density profiles. The hot gas halo density models are marked with dashed curves, and the gaseous disc density models in the plane ($z = 0$ kpc) with solid curves. We show the set-up (i) with yellow curves, i.e. the MW hot halo beta model (Salem et al. 2015) and the gaseous disc (Kalberla & Kerp 2009), and the set-up (ii) (time-varying hot halo density and cold gas disc) at two times: −7.5 Gyr (dark violet) and −10 Gyr (light violet). For comparison, we show a hot halo model from Miller & Bregman (2015) in green. The vertical dotted line marks the current distance of Leo T.

where $\rho_{\text{gas}}^{\text{medium}}$ is the gas density of the interstellar or intergalactic medium of the host galaxy (MW), through which the satellite moves with a velocity V. We consider the following two scenarios for the gas density of the MW (see Fig. 3):

(i) Set-up (i): In this set-up, we use the MW H I disc model from Kalberla & Kerp (2009; see their fig. 4). This is an exponential disc with a shift of 9.8 kpc, a scale of 3.15 kpc, and a central density of $n_{\text{o}}^{\text{H I}} = 0.9$ cm^{-3}. It has a flaring vertical exponential profile with a scale of $h_{\text{o}} = 0.15$ kpc that fits well the radial and vertical H I distribution between 5 and 35 kpc, beyond which the H I disc becomes faint. We assign a rotational velocity to the gaseous disc assuming that it rotates with the same speed as the circular velocity derived from the total gravitational MW potential. The direction of rotation is the same as in the MW, a clockwise rotation in the Galactocentric frame. For the corona or hot halo gas density profile, we use the fiducial beta model from Salem et al. (2015). We note that the hot halo density is carved out where the gaseous disc density is larger, and vice versa. We use then this medium to calculate the ram-pressure variable $P_{\text{R,1}}$ along each orbit.

(ii) Set-up (ii): We consider a time-varying gas density medium with parameters motivated by the NIHAO simulations (Wang et al. 2016). Here we set a hot gas halo density profile that follows the dark matter distribution in the outer parts with a hot gas-to-dark matter mass ratio of 0.16.[2] For the cold gaseous disc, we use a Miyamoto–Nagai gas disc with a scale length and height of 2.5 and 0.1 kpc, respectively, but we set up an extreme scenario where the gaseous disc also contains the mass of the stellar disc (5.5×10^{10} M$_{\odot}$). The assumption here is that at a high redshift, most of the baryons were in the form of gas. Given that the MW H I disc

[2]Private communication.

beyond 35 kpc becomes very shallow and that the Miyamoto–Nagai density profile in the plane is still large at large radii (100 kpc,) we reduce the disc density multiplying by a factor $[e^{(-R/R_{\text{o}})^3}]$ with a scale of $R_{\text{o}} = 40$ kpc, resulting in a disc density that equals the hot halo at 70 kpc (see Fig. 3). Additionally, for the cases with MW mass accretion, we vary the gas mass of the gaseous disc and hot halo as a function of redshift, as explained in cases 2 and 4. We use this medium to calculate the ram-pressure variable $P_{\text{R,2}}$. The main differences between both gas model set-ups are that the set-up (i) is constant in time and that it reaches slightly lower densities in the disc, while set-up (ii) evolves with time and in the outer part the hot halo density profile drops faster than the beta model of set-up (i). We note that the density profiles extend beyond the virial radius, and that we adopt a helium-to-hydrogen gas mass ratio of 0.25.

We also tested different MW gas medium models finding results similar for our velocity constraints, considering, for example, for set-up (i) a Miyamoto–Nagai for the H I disc with a mass of 5×10^9 M$_{\odot}$ (BG16) (see also Bovy & Rix 2013) and a scale length of 2.5 kpc and a height of 0.1 kpc, which has an H I density in the centre of the disc 5 times smaller than the adopted exponential disc. We also tested the MW hot halo model from Miller & Bregman (2015) where we take the parameters of the most massive hot halo (see Fig. 3). The models explored here have a range of coronal densities similar to other estimations: $n_{\text{H}} \approx 3 \times 10^{-4}$ cm^{-3} at 60 kpc (Belokurov et al. 2017), 1×10^{-4} cm^{-3} at 70–120 kpc (Grcevich & Putman 2009), and $(1.3\text{–}3.6) \times 10^{-4}$ cm^{-3} at 50–90 kpc (Gatto et al. 2013).

Now we need to calculate the thermal pressure that allows the satellite to retain its gas. For this, we use the estimate of Mori & Burkert (2000), where the thermal pressure is

$$P_{\text{T}} = \frac{G\, M_{\text{o}}\, \rho_{\text{core}}^{\text{sat}}}{3 r_{\text{core}}} \tag{4}$$

with G being the gravitational constant and $\rho_{\text{core}}^{\text{sat}}$ is the central gas density of the satellite, where we use the value from our Plummer fit $\rho_{\text{Pl}}^{\text{gas}}$. The scale of the dwarf's dark matter core is r_{core}, which we approximate by using the de-projected stellar half-light radius $r_{\text{h}} = 4/3 R_{\text{h}}^{\text{V}}$. This is motivated by dwarf galaxy formation simulations that show that a bursty star formation can generate a dark matter cored with a similar size to the stellar distribution (Ogiya et al. 2014; Read et al. 2016). M_{o} is the dynamical mass within r_{core}, where we use the virial relation (Wolf et al. 2009)

$$M_{\text{half}}^{\text{dyn}} = 3 G^{-1} (4/3) R_{\text{h}}^{\text{V}} \sigma_{\text{los},\star}^2 \tag{5}$$

and the stellar dispersion $\sigma_{\star}$ (Simon & Geha 2007), finding with the latest distance estimate a dynamical mass within the half-light radius of $M_{\text{half}}^{\text{dyn}} = 7.6 \pm 3.3 \times 10^6$ M$_{\odot}$. This gives us a thermal pressure of $P_{\text{T}} = 1.0 \times 10^9$ M$_{\odot}$ kpc^{-3} km^2 s^{-2}.

Additionally, Mori & Burkert (2000) analyse the Kelvin–Helmholtz (KH) instability gas stripping process of a satellite that moves in the host's medium. This mechanism is not instantaneous; it operates cumulatively with time, stripping the gas of the satellite within a given time-scale. Nulsen (1982) finds that the gas mass-loss rate of a satellite through the KH instability is

$$\frac{\text{d}M_{\text{gas}}}{\text{d}t} = \pi r_{\text{core}}^2\, \rho_{\text{gas}}^{\text{medium}}\, V. \tag{6}$$

Therefore, as an additional parameter to estimate the gas stripping for each orbit we re-formulate the previous equation as

$$M_{\text{gas}}^{\text{Orbit}} = \int \text{d}M_{\text{gas}} = \int \pi r_{\text{core}}^2\, \rho_{\text{gas}}^{\text{medium}}\, V \text{d}t, \tag{7}$$
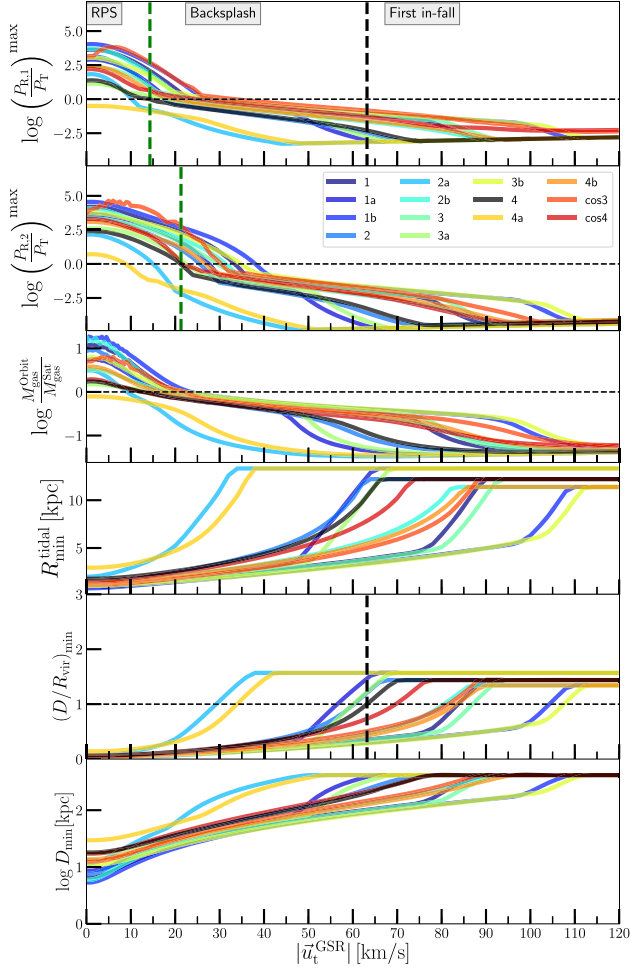
Figure 4. The main parameters taking the median of the parameter for different directions of $\vec{u}_t^{GSR}$ and for different cases (see Table 2) as a function of $|\vec{u}_t^{GSR}|$. See the main text in Section 4.1 for the definitions of the parameters. Each coloured line corresponds to a case labelled in the second top panel, where we note that our fiducial case 4 (accreting MW and M31 potential) is shown in black. From this figure, we identify three main regions in $\vec{u}_t^{GSR}$: (i) the region RPS where the MW ram pressure is larger than the thermal pressure of the satellite. Each direction and case have a slightly different value of $|\vec{u}_{tRPS}^{GSR}|$. We mark the median of P_R of our fiducial case 4 taking all directions of the tangential velocities, finding $|\vec{u}_t^{GSR}| = 14^{+26}_{-14} \, \text{km s}^{-1}$ for $P_{R,1}$ (top panel) and $21^{+33}_{-21} \, \text{km s}^{-1}$ for $P_{R,2}$ (second panel) (dashed green vertical lines). The error range considers the maximum and minimum threshold velocity values found among different directions of $\vec{u}_t^{GSR}$ and different cases. (ii) The backsplash region with orbits that passed through the MW dark matter halo, which we mark for case 4 at the median value and range of $|\vec{u}_t^{GSR}| = 63^{+47}_{-39} \, \text{km s}^{-1}$ (dashed black vertical line); and (iii) the first infall region where orbits never entered the halo. We present the complete results for different directions of $\vec{u}_t^{GSR}$ in Fig. A3.

where, in practice, we just compute the amount of MW gas collected along the orbit within a tube with a radius of $r_{core} = 300 \, \text{pc}$, which represents roughly the radius of the Leo T H I distribution: M_{gas}^{Orbit}. Surviving gas-rich satellites have orbits where $M_{gas}^{Orbit}/M_{gas}^{Sat} < 1$. Of course, this would be an upper limit, under the assumption that the satellite's gas has not changed much. If we include the gas that formed the stars in the past, we would have $M_{gas}^{Orbit}/(M_{gas}^{Sat} + M_{sat}^{\star}) < M_{gas}^{Orbit}/M_{gas}^{Sat} < 1$. Note that the comparison between the gas mass of the satellite and the mass collected along the orbits is approximately

equivalent to a comparison between the gas column density of the satellite and the ambient gas column density along the orbit within the area $\pi \, r_{core}^2$.

4 RESULTS

We present our main results in Section 4.1, with a further analysis of the backsplash orbital solutions in Section 4.1.1 and the gas stripped solutions in Section 4.1.2, including examples of orbits. This is followed by Section 4.2, where we explore in more detail the effects of the cosmic expansion in the orbital calculation. In Section 4.3, we explore the effects of dynamical friction and tidal disruption in the orbital calculation with *N*-body simulations. Finally, we apply our method to other distant dwarfs, presenting these results in Section 4.4.

4.1 Three main orbital solutions

We analyse a total of 4218 orbits for Leo T, which includes all set-up cases for the gravitational potential and different directions and magnitudes of the tangential velocity $\vec{u}_t^{GSR}$. For each orbit, we measure the following seven variables as a function of $|\vec{u}_t^{GSR}|$:

(1) $(D/R_{vir})_{min}$: the minimum of the ratio of the distance between the satellite and the MW centre and the MW virial radius.

(2) $P_{R,1}^{max}/P_T$: the maximum of the ratio of the ram pressure for each orbit considering the set-up (i) for MW gas model and the thermal pressure of the satellite.

(3) $P_{R,2}^{max}/P_T$: same ram-pressure parameter but for the set-up (ii) MW gas model.

(4) $M_{gas}^{Orbit}/M_{gas}^{Sat}$: the ratio of the total gas mass collected along each orbit and the satellite's gas mass.

(5) R_{min}^{tidal}: the minimum tidal radius of the satellite.

(6) D_{min}: the minimum distance of the satellite's orbit to the MW centre.

(7) PA $(\Delta R = 0.1°)$: measures the position angle at a point in the trajectory of the orbit on the sky at $\Delta R = 0.1°$ from the current sky position of Leo T.

The main trend of each variable as a function of $|\vec{u}_t^{GSR}|$ is shown in Fig. 4 with the median of the distributions taken for different directions of $\vec{u}_t^{GSR}$. The values for each direction of $\vec{u}_t^{GSR}$ are shown in Fig. A3. Using now these parameters, we can determine if each orbit is a first infall orbital solution, a backsplash orbital solution, or a gas stripped backsplash orbital solution.

4.1.1 Backsplash and first infall orbital solutions

We can classify each orbit as backsplash if the satellite entered the MW dark matter halo in the past and $(D/R_{vir})_{min} \leq 1$ or as a first infall orbit if $(D/R_{vir})_{min} > 1$. In Fig. 5, we present as an example a set of orbits in a direction of $\vec{u}_t^{GSR}$ for our fiducial case 4, i.e. the set-up that includes the potentials of an accreting MW and the M31 potential. It shows that there is a range of orbits with $|\vec{u}_t^{GSR}| < 65 \, \text{km s}^{-1}$ where the satellite entered the (time-varying) virial radius of the MW between -8 and -12 Gyr ago, while for larger velocities there are found only first infall solutions. Therefore, for each direction of $\vec{u}_t^{GSR}$, there is a particular value of $|\vec{u}_t^{GSR}|$, a threshold $|\vec{u}_{tBAS}^{GSR}|$, below which all orbits are backsplash solutions and $(D/R_{vir})_{min} \leq 1$, finding a similar threshold value when we examine different directions and different cases (see case 1 in Fig. A2).

We can more easily see the main trend of $(D/R_{vir})_{min}$ as a function of $|\vec{u}_t^{GSR}|$ for different cases with the median of $(D/R_{vir})_{min}$ for different
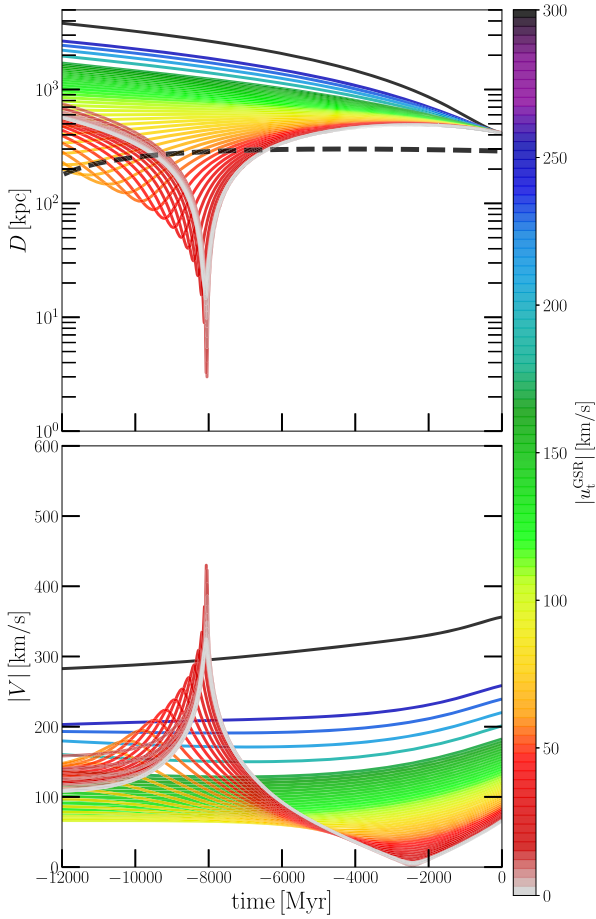
Figure 5. Galactocentric distance (top panel) and velocity (bottom panel) as a function of lookback time for case 4. Colours indicate the value of $|\vec{u}_t^{\mathrm{GSR}}|$, showing only orbits pointing in the direction of PA = 3° to avoid an overcrowding of lines. In the top panel, we show R_{vir} as a function of time (curved dashed line). All orbits that go within R_{vir} are by definition backsplash orbits, while the ones that remain outside are first infall orbits.

directions of $\vec{u}_t^{\mathrm{GSR}}$, which is shown in Fig. 4. In the figure, we can identify the threshold value for the median $\langle |\vec{u}_{t\mathrm{BAS}}^{\mathrm{GSR}}| \rangle$ below which we find the backsplash solutions. The values for each direction are shown in Fig. A3, where we find values of $|\vec{u}_{t\mathrm{BAS}}^{\mathrm{GSR}}|$ that can be larger and smaller than the medians.

In Table 3, we summarize our main results, showing the median threshold values for different cases, as well as the maximum and minimum values found among different directions of $\vec{u}_t^{\mathrm{GSR}}$. From our fiducial case 4, we obtain that orbits with tangential velocities lower than $\langle |\vec{u}_t^{\mathrm{GSR}}| \rangle \leq 62^{+49}_{-38}$ km s^{-1} result in backsplash solutions, where the error range corresponds to the maximum and minimum values found for different cases and directions. The minimum distance is at the backsplash orbital threshold that occurred at $t\left(D_{\mathrm{min}}^{\mathrm{BAS}}\right) = -11.9^{+0.3}_{-0.1}$ Gyr. We discuss how this changes when we include the cosmic expansion in Section 4.2. We also provide the values of $|\vec{u}_{t\mathrm{BAS}}^{\mathrm{GSR}}|$ when we choose the PA directions that better align with the H I morphology, as explained in Section 4.1.4. In Table 3, we find that the largest variations in the exact value of $|\vec{u}_{t\mathrm{BAS}}^{\mathrm{GSR}}|$ are due to the variations of the virial mass of the MW. When we compare subcases (a) and (b), we can see that the threshold increases and decreases by a factor of 2. This is simply because the potential of a more (or less) massive halo will require larger (or smaller) velocities to obtain

orbits that do not enter the virial radius, and also because the virial radius of a more (or less) massive halo is larger (or smaller).

The second important effect comes from the MW accretion history, followed by the M31 potential. For example, in Table 3, the largest value of $|\vec{u}_{t\mathrm{BAS}}^{\mathrm{GSR}}|$ is for case 3b with a constant and large value of $M_{\mathrm{vir}} = 1.6 \times 10^{12} \, \mathrm{M}_\odot$, needing then a larger velocity to obtain first infall solutions. The smallest $|\vec{u}_t^{\mathrm{GSR}}|$ is for case 2a, where M_{vir} is the lowest, and furthermore, it decreases with redshift. The effects of M31 are noticeable when comparing the tangential velocity threshold between cases 1 and 3, where the velocity thresholds are larger for case 3 due to the contribution of the M31's potential. However, the MW virial mass still plays the major role. This provides our first constraint for the tangential velocity. We see in Figs 4 and A3 that the curves of $(D/R_{\mathrm{vir}})_{\mathrm{min}}$ become almost flat for $|\vec{u}_t^{\mathrm{GSR}}| > |\vec{u}_{t\mathrm{BAS}}^{\mathrm{GSR}}|$. This is simply because we enter the region of first infall solutions, and the minimum values correspond to the current position of Leo T.

It is also possible to see in Fig. 5 that the maximum distance of the backsplash orbits is between $D = 1 R_{\mathrm{vir}}$ and $D \sim 4 \times R_{\mathrm{vir}}$ at a lookback time of -12 Gyr (or $z = 3.51$). This value could be even larger in units of the virial radius if we integrate to higher redshifts, given that R_{vir} decreases as well, because the halo mass decreases with redshift, as described by equation (2). This range of distances of backsplash orbits is similar to the satellites in the NIHAO cosmological MW-type simulations (see fig. 7 in Buck et al. 2019). In Section 4.2, we will also show backsplash orbits when we include the cosmic expansion.

4.1.2 Gas stripped orbital solutions

In Fig. 6, we show the ram pressure for different orbits of case 4 as a function of time and $|\vec{u}_t^{\mathrm{GSR}}|$ for a particular direction. In general, we find that for different cases and different directions of $\vec{u}_t^{\mathrm{GSR}}$, the ram pressure of the orbits is quantitatively and qualitatively similar. As expected, the largest ram-pressure values happen for the most radial orbits of the backsplash solutions, with a maximum of $(P_R/P_T)^{\mathrm{max}} \sim 10^4$ larger than the thermal pressure of the satellite. We also compare both MW gas model set-ups, where we see that the ram pressure of the set-up (ii) MW gas model ($P_{R,2}/P_T$) reaches slightly larger values in the centre than with the set-up (i) ($P_{R,1}/P_T$). The first infall solutions experience the largest ram pressure at the current position of Leo T or in some solutions at the apocentres of orbits that passed near but outside of the virial radius.

Similarly to our backsplash analysis, we can classify an orbit as gas stripped if the instantaneous ram pressure overcomes the thermal pressure of the satellite, i.e. $(P_R/P_T)^{\mathrm{max}} \geq 1$, or as unstripped if $(P_R/P_T)^{\mathrm{max}} < 1$. We note that in our set-ups, because the largest MW gas density is in the centre, all the ram-pressure-stripped orbital solutions are also backsplash solutions. The only non-backsplash ram-pressure-stripped solutions would be first infall orbits with extremely large tangential velocities ($|\vec{u}_t^{\mathrm{GSR}}| > 3000$ km s^{-1}).

In Fig. 4, we show the median of $(P_R/P_T)^{\mathrm{max}}$ for different cases as a function of $|\vec{u}_t^{\mathrm{GSR}}|$, showing the values for different directions of $\vec{u}_t^{\mathrm{GSR}}$ in Fig. A3. We can also find a tangential velocity threshold, below which we find only ram-pressure-stripped orbital solutions (RPS), providing a second criterion to constrain the tangential velocity, namely $|\vec{u}_{t\mathrm{RPS}}^{\mathrm{GSR}}|$. Interestingly, we find that this threshold does not change much depending on the MW gas model. In fact, our tests with other MW gas distributions (Section 3.3) result in similar threshold values. This results from the ram pressure depending linearly with the density medium and quadratically with the velocity. When the satellite reaches the central regions ($R < 40$ kpc) and hits the MW

Table 3. Orbital constraints for Leo T.

1	2	3	4	5	6	7	8	9	10	11	12	13
	$\langle|\vec{u}_{\rm t\,BAS}^{\rm GSR}|\rangle$	$\langle D_{\rm min}^{\rm BAS}\rangle$	$|\vec{u}_{\rm t\,BAS}^{\rm GSR}|$	$D_{\rm min}^{\rm BAS}$	$\mu_{\alpha*}^{\rm BAS}$	$\mu_\delta^{\rm BAS}$	$\langle|\vec{u}_{\rm t\,RPS}^{\rm GSR}|\rangle$	$\langle D_{\rm min}^{\rm RPS}\rangle$	$|\vec{u}_{\rm t\,RPS}^{\rm GSR}|$	$D_{\rm min}^{\rm RPS}$	$\mu_{\alpha*}^{\rm RPS}$	$\mu_\delta^{\rm RPS}$
Case	km s⁻¹	kpc	km s⁻¹	kpc	mas yr⁻¹	mas yr⁻¹	km s⁻¹	kpc	km s⁻¹	kpc	mas yr⁻¹	mas yr⁻¹
1	83^{+2}_{-2}	288	84 (83)	287 (287)	$-0.0164\,(-0.0017)$	$-0.1587\,(-0.1561)$	33^{+13}_{-19}	43^{+16}_{-20}	41 (33)	52 (43)	$-0.0157\,(-0.0096)$	$-0.1365\,(-0.1319)$
1a	56^{+2}_{-3}	264	56 (55)	263 (263)	$-0.016\,(-0.006)$	$-0.1446\,(-0.1428)$	27^{+14}_{-16}	39^{+18}_{-17}	35 (27)	49 (39)	$-0.0156\,(-0.0106)$	$-0.1336\,(-0.129)$
1b	104^{+2}_{-2}	308	104 (103)	308 (308)	$-0.0168\,(0.0016)$	$-0.1693\,(-0.1662)$	38^{+12}_{-20}	46^{+15}_{-15}	45 (38)	55 (46)	$-0.0158\,(-0.0088)$	$-0.1389\,(-0.1342)$
2	60^{+2}_{-2}	197^{+2}_{-5}	60 (59)	194 (195)	$-0.016\,(-0.0054)$	$-0.1467\,(-0.1447)$	25^{+8}_{-14}	44^{+11}_{-20}	31 (26)	52 (44)	$-0.0155\,(-0.0108)$	$-0.1314\,(-0.1281)$
2a	29^{+2}_{-3}	164^{+2}_{-2}	29 (28)	164 (164)	$-0.0155\,(-0.0104)$	$-0.1306\,(-0.1295)$	15^{+4}_{-9}	38^{+6}_{-13}	18 (15)	44 (38)	$-0.0153\,(-0.0125)$	$-0.1251\,(-0.1229)$
2b	80^{+2}_{-2}	244^{+2}_{-7}	81 (80)	242 (242)	$-0.0164\,(-0.0022)$	$-0.1571\,(-0.1547)$	31^{+8}_{-17}	46^{+11}_{-22}	37 (31)	55 (47)	$-0.0157\,(-0.0099)$	$-0.1346\,(-0.131)$
3	87^{+4}_{-12}	288	91 (91)	287 (287)	$-0.0166\,(-0.0004)$	$-0.1624\,(-0.16)$	29^{+21}_{-16}	38^{+21}_{-15}	48 (41)	54 (43)	$-0.0158\,(-0.0083)$	$-0.1403\,(-0.1358)$
3a	60^{+7}_{-11}	264	67 (67)	263 (263)	$-0.0162\,(-0.0042)$	$-0.15\,(-0.1483)$	22^{+24}_{-14}	34^{+24}_{-11}	43 (36)	52 (40)	$-0.0158\,(-0.0091)$	$-0.138\,(-0.1334)$
3b	107^{+3}_{-12}	308	109 (109)	308 (308)	$-0.0169\,(0.0025)$	$-0.1716\,(-0.169)$	34^{+19}_{-19}	41^{+19}_{-17}	52 (45)	56 (46)	$-0.0159\,(-0.0077)$	$-0.1423\,(-0.1378)$
4	63^{+6}_{-2}	201^{+15}_{-2}	69 (69)	209 (209)	$-0.0162\,(-0.0039)$	$-0.151\,(-0.1492)$	21^{+18}_{-12}	38^{+17}_{-13}	39 (34)	54 (45)	$-0.0157\,(-0.0094)$	$-0.1357\,(-0.1324)$
4a	33^{+9}_{-10}	164^{+2}_{-2}	43 (43)	164 (164)	$-0.0158\,(-0.0081)$	$-0.1376\,(-0.1364)$	8^{+22}_{-8}	34^{+16}_{-9}	30 (26)	49 (39)	$-0.0155\,(-0.0107)$	$-0.1313\,(-0.1286)$
4b	83^{+4}_{-12}	245^{+13}_{-3}	87 (87)	257 (256)	$-0.0165\,(-0.001)$	$-0.1603\,(-0.158)$	26^{+18}_{-14}	39^{+18}_{-14}	44 (39)	56 (47)	$-0.0158\,(-0.0086)$	$-0.1383\,(-0.1348)$
cos3	81^{+4}_{-11}	288	81 (81)	287 (287)	$-0.0164\,(-0.0019)$	$-0.1573\,(-0.1555)$	31^{+11}_{-21}	51^{+13}_{-21}	41 (38)	59 (54)	$-0.0157\,(-0.0089)$	$-0.1366\,(-0.1341)$
cos4	69^{+4}_{-2}	284^{+2}_{-2}	73 (73)	287 (286)	$-0.0163\,(-0.0032)$	$-0.1532\,(-0.1513)$	21^{+17}_{-12}	42^{+21}_{-14}	38 (33)	59 (49)	$-0.0157\,(-0.0097)$	$-0.135\,(-0.1317)$
B.V.	63	201	69 (69)	209 (209)	$-0.0162\,(-0.0039)$	$-0.151\,(-0.1492)$	21	38	39 (34)	54 (45)	$-0.0157\,(-0.0094)$	$-0.1357\,(-0.1324)$
$\pm\Delta$	$^{+47}_{-39}$	$^{+107}_{-36}$	$^{+39}_{-44}\,(^{+40}_{-44})$	$^{+98}_{-44}\,(^{+99}_{-44})$	$^{+0.0007}_{-0.0007}\,(^{+0.0065}_{-0.0065})$	$^{+0.0204}_{-0.0206}\,(^{+0.0197}_{-0.0198})$	$^{+33}_{-21}$	$^{+26}_{-16}$	$^{+12}_{-20}\,(^{+10}_{-19})$	$^{+5}_{-9}\,(^{+9}_{-6})$	$^{+0.0003}_{-0.0002}\,(^{+0.0017}_{-0.0031})$	$^{+0.0106}_{-0.0066}\,(^{+0.0095}_{-0.0053})$

Notes. The zero tangential GSR velocity for Leo T ($|\vec{u}_{\rm t}^{\rm GSR}| = 0$ km s⁻¹) corresponds to $\mu_{\alpha*}^\circ = -0.0150$ mas yr⁻¹ and $\mu_\delta^\circ = -0.1153$ mas yr⁻¹. Column 1 corresponds to the case scenario. Columns 2 and 3 list the value of $|\vec{u}_{\rm t}^{\rm GSR}|^{\rm BAS}$ for the median of $(D/R_{\rm vir})_{\rm min}$ for different directions of $\vec{u}_{\rm t}^{\rm GSR}$, and the minimum distance, below which the orbits are backsplash solutions, with the error range taken from the threshold values for different directions of $\vec{u}_{\rm t}^{\rm GSR}$ or from the grid resolution. Columns 4–7 correspond to the backsplash solutions of our grid that are close to the direction of $PA_{\rm offset}=3°$, where we show the velocity, the minimum distance, and the proper motion. In brackets we show the solutions close to the direction of $PA_{\rm flat}=-21°$. Columns 8 and 9 are the value of $|\vec{u}_{\rm t}^{\rm GSR}|^{\rm RPS}$ and the minimum distance when we take the median of $P_{\rm R,2}/P_{\rm T}$ for different directions of $\vec{u}_{\rm t}^{\rm GSR}$. Below this value, the orbits are ram-pressure-stripped solutions, with the error range taken from the different directions of $\vec{u}_{\rm t}^{\rm GSR}$ or from the grid resolution. Columns 10–13 correspond to the RPS solutions of $\vec{u}_{\rm t}^{\rm GSR}$ closest to the direction $PA_{\rm offset}$, showing the values $|\vec{u}_{\rm t}^{\rm GSR}|$, minimum distance, and the proper motions. In brackets we include the values for the direction of $PA_{\rm flat}$. The last two rows: B.V. are the best values selected from our fiducial scenario case 4 with errors taken from the range of maximum and minimum values from different cases, including the range for different directions of $\vec{u}_{\rm t}^{\rm GSR}$.
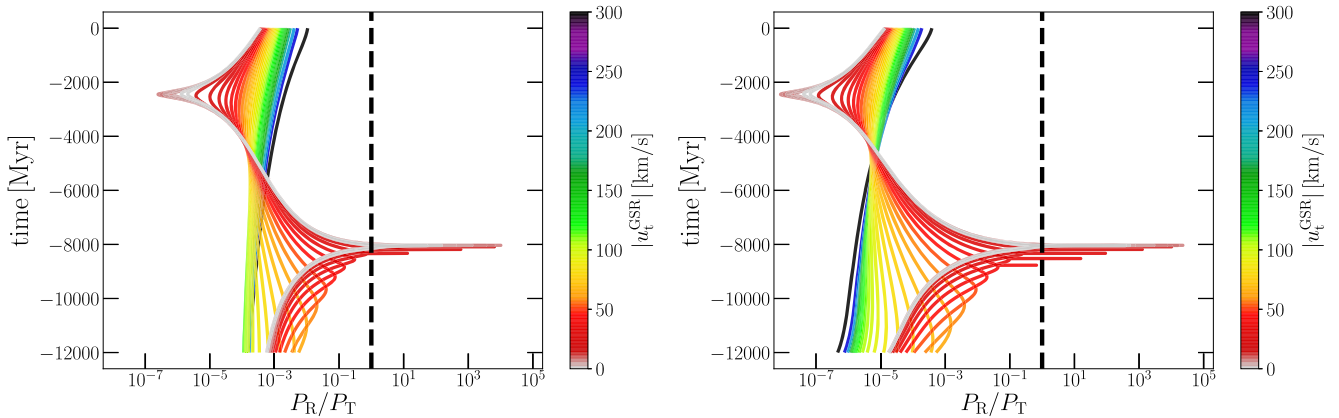

Figure 6. Ram pressure-to-thermal pressure ratio as a function of time for case 4, calculated for the set-up (i) of the MW gas medium $P_{\rm R,1}$ (left-hand panel) and the set-up (ii) $P_{\rm R,2}$ (right-hand panel). Colours indicate the value of $|\vec{u}_{\rm t}^{\rm GSR}|$, showing here only orbits pointing in the direction of $PA = 3°$ to avoid an overcrowding of lines. A ratio of $P_{\rm R}/P_{\rm T} = 1$ is marked with a vertical dashed line. Ratios larger than one denote the region where the gas of the satellite would be stripped by the MW.

gaseous disc, it already has a large velocity, between 200 and 400 km s⁻¹ (see Fig. 5; or up to 500 km s⁻¹ in case 1; Fig. A2), which increases the ram pressure quadratically.

In Table 3, we present the median threshold values for different cases, finding, for example, for our fiducial case 4 that backsplash solutions with $\langle|\vec{u}_{\rm t\,RPS}^{\rm GSR}|\rangle > 21^{+33}_{-21}$ km s⁻¹ would allow Leo T to survive the ram-pressure stripping of the MW, with wide orbits that have a minimum distance of $D_{\rm min} \geq 38^{+26}_{-16}$ kpc. The error range considers different directions of $\vec{u}_{\rm t}^{\rm GSR}$ and different cases. We note that in Table 3 we show the threshold values obtained from the MW gas set-up (ii), because the threshold value is slightly larger than that with the set-up (i). The minimum distance is at the ram-pressure threshold that occurred at $t\left(D_{\rm min}^{\rm RPS,2}\right) = -8.4^{+0.2}_{-0.4}$ Gyr. We discuss how this changes when we include the cosmic expansion in Section 4.2. We

also show in the table the threshold $|\vec{u}_{\rm t\,RPS}^{\rm GSR}|$ for directions that better align with different features in the H I morphology, as explained in Section 4.1.4.

Similarly to the backsplash analysis, in the table we also find that the largest variations of $|\vec{u}_{\rm t\,RPS}^{\rm GSR}|$ arise from differences in the total mass of the MW, and from the MW accretion history. Particularly, the latter determines the potential in the MW centre, which can bring the orbits of the satellites closer to the MW centre where the gas is denser, which then pushes region of the ram-pressure solution to larger values of $|\vec{u}_{\rm t\,RPS}^{\rm GSR}|$. However, even when comparing extreme cases, such as case 1 with the static MW potential and case 2 with the accreting MW, we see that $|\vec{u}_{\rm t\,RPS}^{\rm GSR}|$ values agree within their ranges.

And finally, we also find that the cumulative gas stripping through the KH instability could strip very radial orbits, but it is subdominant

when compared to the ram pressure (see Section 3.3). In Figs 4 and A3, we show that the amount of gas collected along each orbit is larger than the gas in Leo T only for very radial orbits, which are already within the ram-pressure-stripped region. This implies that, in this particular scenarios, the KH instability, parametrized as in equation (7), would be less efficient than the instantaneous ram-pressure stripping to remove the gas of the dwarf.

4.1.3 Tidally disrupted orbits

We calculate this quantity according to equation (1), and assuming a total virial mass for the satellite of $10^8 \, M_\odot$, based on dwarf galaxy formation models in isolation (Read et al. 2016). Changing this to 10^7 or $10^9 \, M_\odot$ would imply a change of the tidal radius only by a factor of ~2 smaller or larger, respectively. As shown in Figs 4 and A3, the value is large enough ($R_{\min}^{\rm tidal} > 1 \, \rm kpc$) to avoid the complete disruption of the satellite in the region of $|\vec{u}_t^{\rm GSR}| > 20 \, \rm km \, s^{-1}$. This is corroborated with our N-body simulations in Section 4.3, where only the outer layers of the dark matter distribution of the dwarf could be stripped, leaving a core that can keep the stellar component of the dwarf bound.

4.1.4 The trajectory of Leo T on the sky and proper motion constraints

In the previous sections, we determined constraints for the magnitude of the tangential velocity considering several directions of $\vec{u}_t^{\rm GSR}$. Here, we constrain the direction of $\vec{u}_t^{\rm GSR}$ by comparing the orientation of the orbits of Leo T projected on the sky with several gas features in Leo T (Fig. 1) that we discuss in Section 2.

Particularly, we search for orbits that are aligned with the H I-stellar offset at $\rm PA_{offset} = 3°$, the H I tail at $\rm PA_{tail} = -10°$, and the H I flattening at $\rm PA_{flat} = -21°$. We argue in Section 2 that these features could be produced by the ram pressure from the MW gas halo, which would generate the tail and the offset that would be aligned with the projected orbit of Leo T, and the flattening of the H I isophotes to the South of Leo T, which would be perpendicular to the projected orbit.

Under this assumption, we vary the direction of the tangential velocity $\vec{u}_t^{\rm GSR}$ to find the best alignment of the projected orbit with this offset axis. In Fig. 7, we show some orbits of our fiducial case, case 4, which are projected on the sky together with the H I map of Leo T, where we show a range of directions and magnitudes for $\vec{u}_t^{\rm GSR}$. The figure shows how the orbits start bending in the direction of the most radial orbits when the values of $|\vec{u}_t^{\rm GSR}|$ decrease below $10 \, \rm km \, s^{-1}$. Above this value, the orbits align well with the given direction of $\vec{u}_t^{\rm GSR}$. We also include in Fig. 7 some orbits for a case that does not include the potential of M31 in the calculation (case 2), to illustrate an interesting difference with the cases that do account for M31: Given that the MW and Leo T have different accelerations towards M31, the resulting orbits are slightly different to that of the cases without M31. This effect is mostly noticeable for the most radial orbits with $|\vec{u}_t^{\rm GSR}| < 1.5 \, \rm km \, s^{-1}$, where for case 4 the radial orbits approach from the MW from $\rm PA = -45°$ to Leo T's current position, while in the isolated case 2 the orbits come from $\rm PA = -100°$. We note that in Fig. 7 we have plotted the orbits on the sky from an inertial frame.

To constrain the direction of $\vec{u}_t^{\rm GSR}$, we project all the orbits on the sky as shown in Fig. 7, and then measure the position angle of each orbit where the orbit intersects a ring on the sky with a radius $\Delta R = 0.1°$ (713 pc) centred on the position of Leo T determining $\rm PA \, (\Delta R = 0.1°)$. The result of this measurement is shown in Fig. 8 for case 4. In the plot, we mark all the orbits with
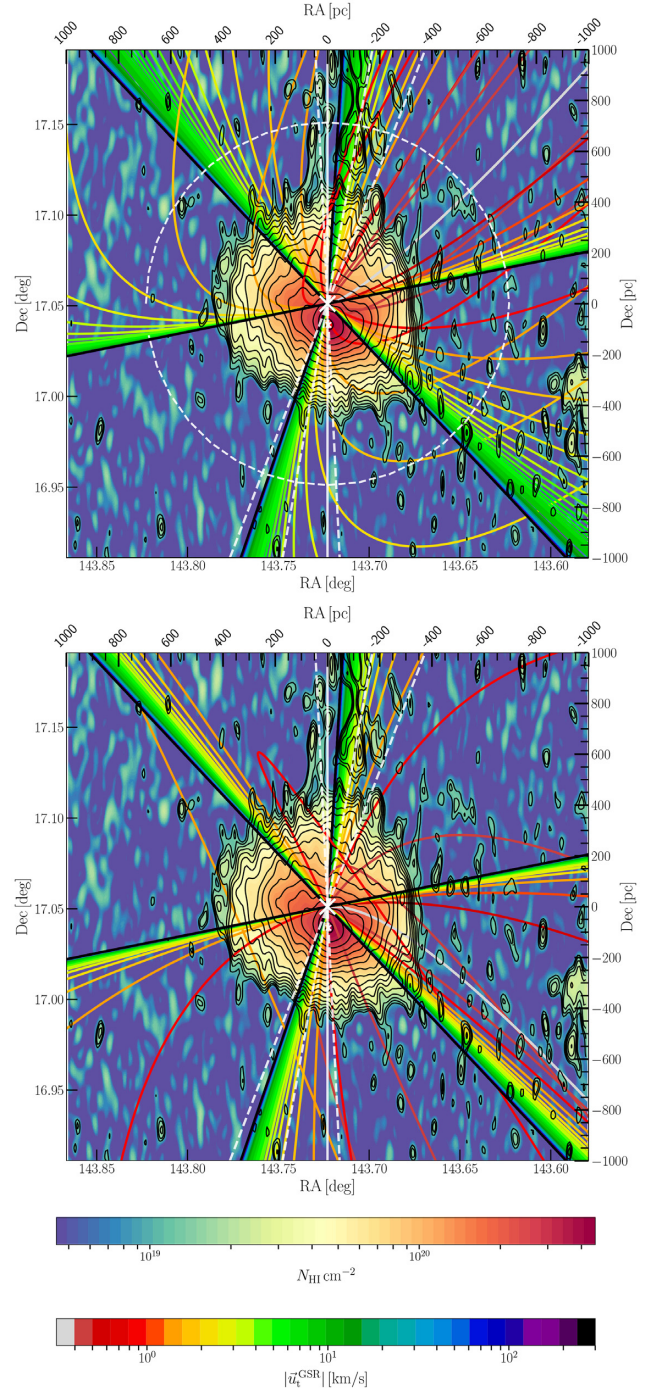

Figure 7. We show orbits of case 4 (top panel) and case 2 (bottom panel) projected on the sky, showing different directions of $\vec{u}_t^{\rm GSR}$ and magnitudes (coloured curves). We also plot the H I column density map and contours of AO18. The optical centre is marked with the large cross, the H I density peak with small cross, and the north–south axis is shown with a white solid vertical line. We plot a circle with $\Delta R = 0.1°$ (713 pc) where we measure the PA of the orbits. Given that we use a logarithmic velocity colour bar, we tag the zero velocity curve ($|\vec{u}_t^{\rm GSR}| = 0 \, \rm km \, s^{-1}$) as the minimum value in the bar ($0.3 \, \rm km \, s^{-1}$) (grey curve). Note the way the orbits bend towards the most radial orbits when $|\vec{u}_t^{\rm GSR}|$ decrease to zero. For case 4, the most radial orbits approach from north-west due to the acceleration towards M31, while in case 2 they approach from south-west.
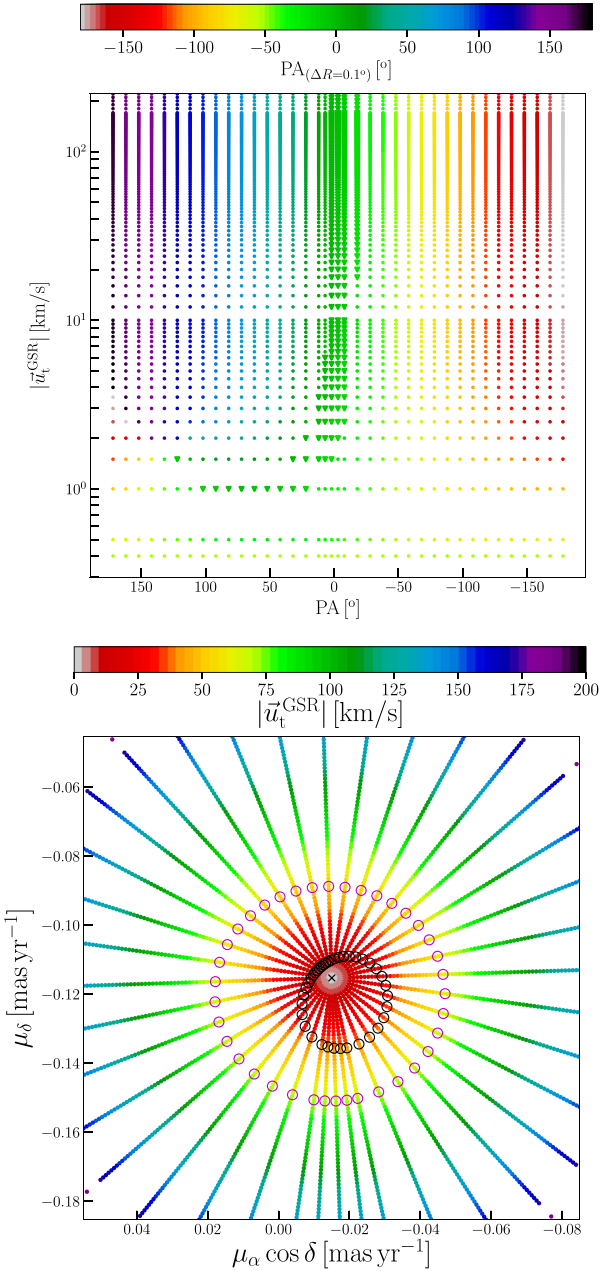
values of PA ($\Delta R = 0.1°$) that fall within the PA$_{offset}$ and PA$_{flat}$. Some solutions are found for larger values of PA ($\sim$50–120°) and very small tangential velocities of $|\vec{u}_t^{GSR}| \leq 1.5\,\text{km s}^{-1}$, but larger than $0.5\,\text{km s}^{-1}$, because those are very radial orbits, which in projection rapidly bend and turn back in direction to the Galaxy. In Fig. 8, we present the explored proper motions for Leo T as a function of $|\vec{u}_t^{GSR}|$ for case 4. We mark the regions where we obtain backsplash orbital solutions and gas stripped solutions, determined as in Sections 4.1.1 and 4.1.2. The proper motions of the grid that generate orbits that best align with the direction of the H I-stellar offset and the H I flattening are enclosed by the two lines shaping a wedge. We note in the figure that the ram-pressure region is not centred exactly around $|\vec{u}_t^{GSR}| = 0\,\text{km s}^{-1}$. This is because there is some angular momentum, given that $\vec{v}_{los}^{GSR}$ is not exactly equal to the radial velocity in GCs, also due to the potential of M31, which perturbs the orbit, and also to the fact that the satellite 'hits' the gaseous disc on different regions with different densities and at slightly different times.

In Table 3, we provide for different cases the tangential velocity threshold values $|\vec{u}_{tRPS}^{GSR}|$ and $|\vec{u}_{tBAS}^{GSR}|$ for both the directions, the H I-stellar offset and the H I flattening, providing this value as proper motions as well, with the proper motion errors in the table estimated from the different cases. In addition, we take the direction along the H I tail PA$_{tail} = -10°$ that lays between the PA of the H I offset and the flattening, and obtain the proper motion ranges for different orbital solutions. Given that this selection of orbits is almost aligned with the north axis, the proper motion in *DEC* is what mostly determines the region where the solution is:

   (i) first infall solutions for $\mu_\delta < -0.1507$[mas yr^{-1}];
   (ii) unstripped gas backsplash orbital solutions (BAS) are within the range of $-0.1507 \leq \mu_\delta/[\text{mas yr}^{-1}] \leq -0.1347$;
   (iii) backsplash ram-pressure-stripped solutions (RPS) are within the range of $-0.1347 \leq \mu_\delta/[\text{mas yr}^{-1}] \leq -0.1153$.

Furthermore, if the restriction on the direction of the velocity is not imposed, Fig. 8 can provide constraint on the magnitude of the proper motion for case 4.

We note that new proper motion estimates for Leo T were published by McConnachie & Venn (2020). We find that these these values and the observational error region overlaps with our the region of backsplash solutions as well as with the first in-fall solution region, given that the observational errors are large due to the large distance to Leo T. Moreover, we note that our proper motion values estimated from the HI morphology lay within this observational region.

4.2 Effects of the cosmic expansion on the orbits

In this section, we show our orbits calculated backwards in time for Leo T, solving the equations of motion of an expanding Universe, as is explained in Section 3.1.

Karachentsev et al. (2009) show how the kinematics of the galaxies in the LG transitions into the Hubble flow at a distance of $\sim$1 Mpc from the LG centre, denoted as the zero velocity radius (see their fig. 1). They show how at those distances the LG gravitational potential perturbs the kinematics of the galaxies moving in the Hubble flow and, more relevant for this work, it is shown how the Hubble flow perturbs the dynamics of the LG and the distribution of its satellites in the outer regions of the LG. The Peñarrubia et al. (2014) analysis also shows with test particles that the cosmic expansion indeed affects the spatial and kinematical distribution of the satellites located at distances of about the separation between M31 and MW (currently 0.78 Mpc) and larger, dominating the Keplerian potential. At smaller
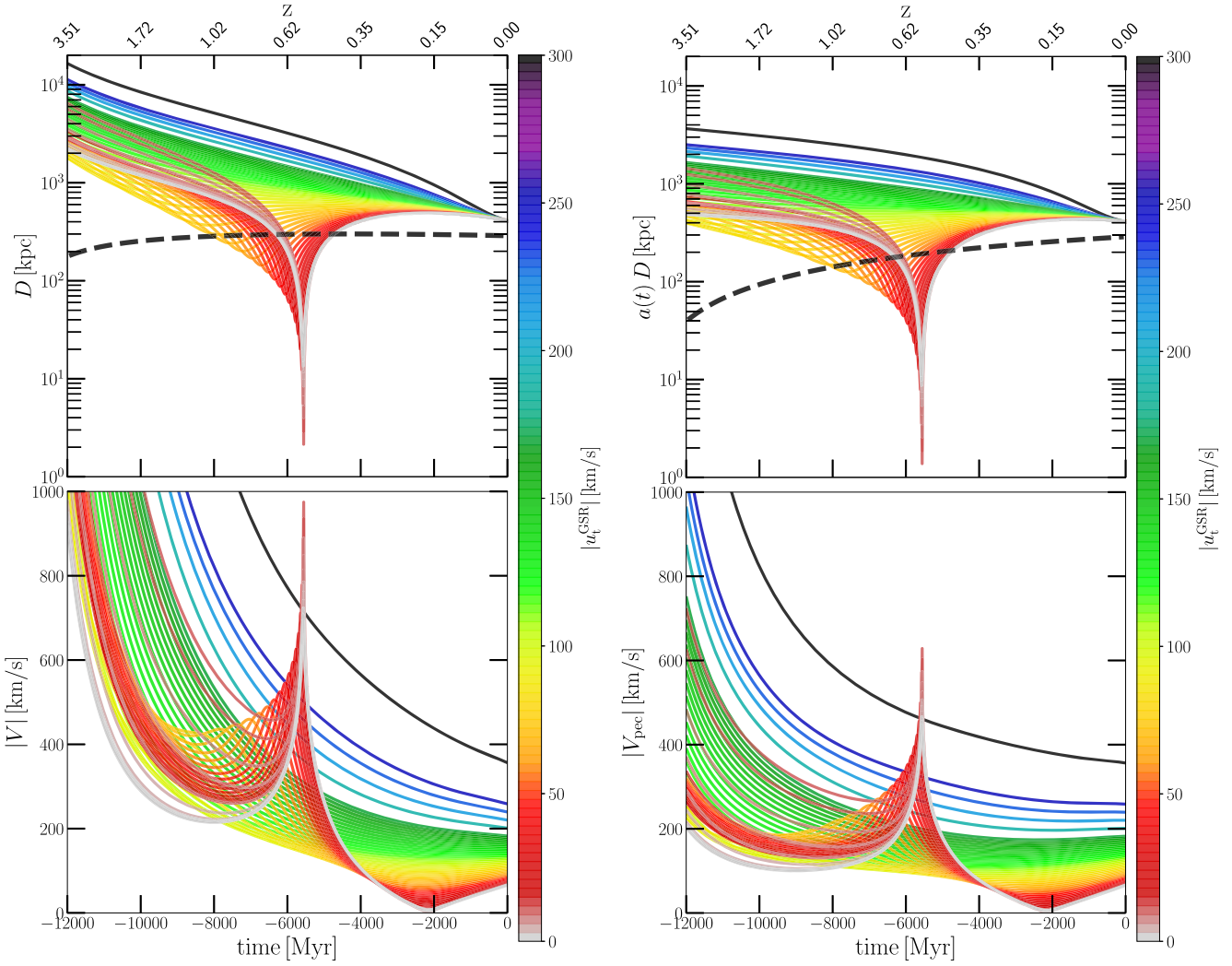
Figure 8. Top panel: direction of the tangential velocity $\vec{u}_t^{GSR}$ as a function of its magnitude $|\vec{u}_t^{GSR}|$ for case 4. Given that the velocity colour bar scale is logarithmic, we have tagged the zero velocity ($|\vec{u}_t^{GSR}| = 0\,\text{km s}^{-1}$) as $0.4\,\text{km s}^{-1}$ in the plot. The colours show the position angle of each orbit where it intersects a circle on the sky with a radius of $\Delta R = 0.1°$ centred on the optical centre of Leo T. The triangle symbols mark the PA values that fall within the position angle of the H I-stellar offset and the H I flattening, with a few degrees of error range, i.e. between PA$_{offset} = 3°$ and PA$_{flat} = -21°$. Bottom panel: proper motions explored for Leo T's current position for case 4 as a function of $|\vec{u}_t^{GSR}|$ (colour bar). The proper motion when $|\vec{u}_t^{GSR}| = 0\,\text{km s}^{-1}$ corresponds to $\mu_{\alpha*} = -0.0150\,\text{mas yr}^{-1}$, $\mu_\delta = -0.1153\,\text{mas yr}^{-1}$ due to the solar motion around the MW (grey region). Each radial set of points corresponds to different directions of $\vec{u}_t^{GSR}$. The values that better align with the H I-stellar offset at PA$_{offset}$ and the H I flattening located at PA$_{flat}$ are located within the black lines shaping a triangle. The black small circles surrounding the centre mark the ram-pressure-stripped region due to $P_{R,2}$, and the magenta circles mark the backsplash solution region.

Figure 9. We show for the case cos4 (case 4 in an expanding space) the comoving Galactocentric distance and velocity (left-hand panels) and the physical coordinate distance and peculiar velocity (right-hand panels) as a function of the lookback time (see Section A2 and equation A7). Colours indicate the value of $|\vec{u}_t^{GSR}|$, showing here only a selection of orbits coming from the direction of PA = 3° to avoid overcrowding. In the top panels is shown the virial radius as a function of time in comoving coordinates (R_{vir}) and physical coordinates (r_{vir}) (curved dashed line).

distances, the quadrupole modes of the potentials contribute in addition to the monopole terms. Hence, the total mass of the LG determines the extension of the influence on the satellites that transition into the Hubble flow. Current LG mass estimates come from the timing argument, where most of the mass is from M31 and the MW. The third most massive galaxy in the LG is the Triangulum galaxy (M33), with an estimated dynamical mass within its H I distribution of $8 \times 10^{10} \, M_\odot$ (Kam et al. 2017). The LG mass ranges in the literature mostly depend on the relative velocity between the M31 and MW systems (BG16). van der Marel et al. (2012) determine a (virial) timing LG mass by selecting galaxy pairs in the Millennium simulations (Li & White 2008) finding $4.9 \pm 1.6 \times 10^{12} \, M_\odot$. After considering the orbit of M33 about M31, they estimate a timing mass of $3.2 \pm 0.6 \times 10^{12} \, M_\odot$. Peñarrubia et al. (2014) estimate a timing LG mass of $2.3 \pm 0.7 \times 10^{12} \, M_\odot$, similar to the values used in our models that include the MW and M31 (cases 3, 4, cos3, and cos4) with a total mass of $M_{tot} = (1.1 + 1.3) \times 10^{12} \, M_\odot = 2.4 \times 10^{12} \, M_\odot$ or in subcases (b) $M_{tot} = 2.7 \times 10^{12} \, M_\odot$, which would then be within that range.

Therefore, dwarfs orbiting at large distances from the LG, such as Leo T or Cetus, located between ~400 and ~700 kpc, can experience deviations on their orbits by the cosmic expansion. We observe this deviation in our orbital calculations, which is better revealed when we compare the distance and velocity of the orbits of our fiducial case 4 in Fig. 5 with the cosmological orbits of case cos4 in Fig. 9, which is case 4 (MW accreting with M31 potentials), but in an expanding space time. In Fig. 9, we show the distance and velocity both in comoving coordinates ($\vec{X}$, $\vec{V}$) and the physical position coordinate $\vec{r}$ and the peculiar velocity is $\vec{V}_{pec}$, which are related by equation (A7), and the parameter $a(t)$ is shown in Fig. A1.

Similarly to other cases, we find that, qualitatively, the properties of the orbits are similar to that of the non-expanding cases, with the most noticeable differences listed here:

(i) We find in Fig. 9 for case cos4 that the distances reached by the backsplash and first infall orbits at −12 Gyr ($z = 3.5$) are larger than those in the non-expanding case, reaching distances between 1 and 5 Mpc in comoving coordinates or 0.4 and 1.5 Mpc in physical coordinates. In units of virial radius, this is roughly $D \sim 10 R_{vir}$ at

that redshift, which is similar to the most distant backsplash orbits found in the NIHAO cosmological MW-type simulations (see fig. 7 in Buck et al. 2019).

(ii) Shift of first pericentre passage: The first pericentre passage in case cos4 for the most radial backsplash orbits coming from large distances is reached at $t = -5.7$ Gyr, resulting in a time delay with a shift of $\Delta t \approx 2$ Gyr later than in the non-expanding fiducial case 4, where the first pericentre passage is at $t = -8.1$ Gyr. We also determined the median and maximum and minimum times for the backsplash threshold orbits for case 4, which is $t\left(D_{\min}^{\mathrm{BAS}}\right) = -11.9_{-0.1}^{+0.3}$ Gyr, and for the ram-pressure threshold is $t\left(D_{\min}^{\mathrm{RPS,2}}\right) = -8.4_{-0.4}^{+0.2}$ Gyr. However, including the cosmic expansion delays these to $t\left(D_{\min}^{\mathrm{BAS}}\right) = -7.5_{-0.6}^{+0.2}$ Gyr and $t\left(D_{\min}^{\mathrm{RPS,2}}\right) = -5.7_{-0.2}^{+0.1}$ Gyr, i.e. a similar delay shift ranging from $\Delta t \approx 3$ to 5 Gyr.

This results from the cosmic expansion at $z > 1$, where the backsplash orbital solutions for this dwarf predict larger distances from the MW at early times, which then take longer to fall to the centre, and also due to the Hubble flow that decelerates the infalling satellite orbits when $H(z)$ is large. Then at closer distances ($D < 2R_{\mathrm{vir}}$) and lower redshift ($z < 1$), the mass accretion of the MW contributes in bringing the first infalling satellites closer to the MW centre after their first infall. We test the effects of the cosmic expansion without the effects of the MW mass accretion or the dark halo extension. For this, we calculate the orbits of Leo T backwards in time considering a Keplerian potential with a constant total mass of $M_{\mathrm{vir}} = 1.3 \times 10^{12}$ M$_\odot$ with and without the cosmic expansion, also finding for the latter a time delay of ~ 2 Gyr.

Also, in Section 4.3 we show our analysis of the effects of dynamical friction on our backsplash orbits with the analytical Chandrasekhar approximation and full *N*-body simulations, which reveal that this mechanism is ineffective in bringing the satellite on backsplash orbits closer to the MW centre when the pericentre distance and the maximum velocity are large.

(iii) The maximum velocity for the most radial orbits is ~ 970 km s^{-1} in comoving velocity V, or ~ 600 km s^{-1} in peculiar velocity, larger than that in the non-expanding space case 4, which reaches ~ 400 km s^{-1}. This results from a combined effect of the dwarf falling from a much larger distance, as well as the first infall time delay that sets the pericentre passage 2 Gyr later, when the MW has accreted more mass, assembling already 90 per cent of its present mass. The latter effect can be seen by comparing with case 1 in Fig. A2, where the MW mass is constant, reaching the satellite at a velocity of up to 500 km s^{-1}.

4.3 Dynamical friction and tidal effects

We test the effects of dynamical friction including the Chandrasekhar approximation on the orbit calculation. We find that cases 5 and 5c behave similarly to the cases without the friction term, with the largest effects for radial orbits that reach the centre where the MW has the highest density. To better estimate the effects of the dynamical friction on our orbits, we set up particle models for Leo T and the MW to run full *N*-body simulations to explore orbits with different tangential velocities.

4.3.1 Initial conditions and set-up

We generate initial conditions for our *N*-body models with the open-source program DICE (Perret et al. 2014; Perret 2016). For the MW, we set up three components with masses and scale parameters according

to case 1 in Section 3.2. For the halo, disc, and spheroid, we use 3×10^6, 1.3×10^5, and 1.2×10^4 particles, respectively. Most orbits studied here have pericentres outside or in the outskirts of the disc and the inner spheroid, making a high number density unnecessary, while the potentials of these components are included.

For Leo T, we model the stellar component with a Plummer profile with a mass of 2×10^5 M$_\odot$ and a de-projected scale of 250 pc. To consider Leo T's gas potential, we also include a particle component for the gas that is modelled only as a collisionless component. We use the parameters of our fitted Plummer to the gas, i.e. a Plummer mass of 5.2×10^5 M$_\odot$ and a de-projected scale of 260 pc. For the dark matter halo, we choose the cored Burkert (1995) and Burkert (2015) profile, which is motivated by dwarf galaxy formation simulations that show that a bursty star formation can generate a cored dark matter profile (Ogiya et al. 2014; Read et al. 2016) with a core the size of the de-projected stellar half-mass radius; here we choose 260 pc. For the dark matter mass, we use the Leo T lowest estimate of Patra (2018) of $M_{\mathrm{DM}}^{0.3\,\mathrm{kpc}} = 2.7 \times 10^6$ M$_\odot$. $M_{\mathrm{o}} = 3.4 \times 10^6$ M$_\odot$ is the dynamical mass within a 300 pc radius that includes the gaseous, stellar, and dark matter masses. We use 5×10^5 particles for the dark matter and 2×10^5 for the gaseous and stellar components, which is enough to prevent an artificial tidal disruption (van den Bosch & Ogiya 2018). Our *N*-body models are not an exact match to Leo T, but sufficient as a metric to estimate the effects of dynamical friction and tidal disruption on our analytical orbits for a Leo T-type galaxy.

We also set up a NFW dark matter halo for Leo T to explore the effects of tidal disruption in a more concentrated profile. Following the main initial condition parameters of Read et al. (2016) for a Leo T-type dwarf, we set up a dwarf galaxy with a virial mass, concentration, and particle number of 5×10^8 M$_\odot$, 24.93, and 10^6, respectively, where the baryonic component parameters are the same as in the cored Leo T model. This model has a dynamical mass within 300 pc of $\sim 10^7$ M$_\odot$ (Fig. A4), as high as estimates from the H I kinematics (Faerman et al. 2013; AO18).

To virialize and relax the initial *N*-body models in isolation, we use the one core tree-code GYRFALCON (Dehnen 2000) from NEMO (Teuben 1995). We relax the *N*-body models for 12 Gyr, where the edges of the dark haloes spread, and in the case of the MW model, the disc develops a bar. For these calculations, the bar orientation and pattern speed are left free, given that the studied orbits are far enough that the quadrupole potential of the bar is weak.

4.3.2 Orbits in frozen and live MW potentials

Our experiments consist of two steps. In the first step, we coupled DELOREAN with GYRFALCON to use the relaxed MW particle model to calculate several orbits for Leo T 12 Gyr backwards in time in a frozen potential as test particles, where the particles of the MW are not allowed to move in time. We explored the values: $|\vec{u}_{\mathrm{t}}^{\mathrm{GSR}}| = (10, 20, 30, 40, 50, 60, 70, 80, 90, 100, 150, 200, 250$ km s$^{-1})$, with a fixed direction of PA $= -5°$ (see Section 4.1.4). In the second step, we use the coordinates and velocities found at -12 Gyr as initial positions and velocities to locate our relaxed *N*-body models of Leo T. Then we proceed to run it forward in time for 12 Gyr until the present ($t = 0$ Gyr), but this time we evolve in time the MW and Leo T particles and potential.

In Fig. 10 are shown the distance and velocity of the orbits for the frozen and live potentials. To calculate the orbits and the relative separation and velocity of Leo T and the MW in the live potentials, we keep track of the centre of mass of the stellar component of Leo T and the MW. In Table 4, we present the difference in position
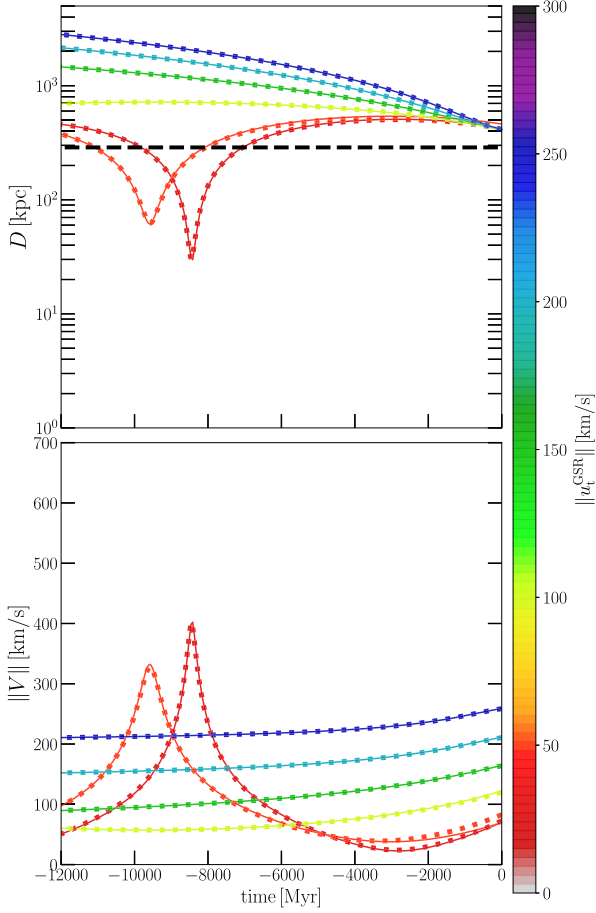
Figure 10. Relative distance and velocity of Leo T relative to the MW as a function of lookback time for the full live *N*-body MW and Leo T simulation shown with solid curves, and for the frozen *N*-body MW potential, shown with dotted curves, almost always overlaying the solid curves. We show results for $|\vec{u}_t^{\rm GSR}| = (30, 50, 100, 150, 200, 250\,{\rm km\,s^{-1}})$ (colours).

Table 4. Orbits in frozen and living *N*-body potentials.

$|\vec{u}_t^{\rm GSR}|[\,{\rm km\,s^{-1}}]$	30	50	100	150	200	30^a	50^a
$D_{\rm L}/D_{\rm F}$	1.01	1.11	0.98	1.0	1.0	0.98	0.99
$\|\vec{D}_{\rm F} - \vec{D}_{\rm L}\|\,{\rm kpc}$	18	52	8	1	0.4	6	4
$\|\vec{V}_{\rm F} - \vec{V}_{\rm L}\|\,{\rm km\,s^{-1}}$	2.3	15	2.9	0.4	0.6	2.1	1.4

Notes. $\vec{V}_{\rm F}$ and $D_{\rm F} = 414\,{\rm kpc}$ are the relative velocity and distance between the satellite and the MW at $t = 0\,{\rm Gyr}$ for the frozen (F) *N*-body potential. $\vec{V}_{\rm F}$ and $D_{\rm L}$ are the same quantities calculated for the living (L) potential.
[a]Values calculated from orbits integrated from an initial condition at $-7\,{\rm Gyr}$ instead of $-12\,{\rm Gyr}$.

and velocity between the orbits in a frozen potential and in a living potential for a selection of tangential velocities. We find that at $t = 0\,{\rm Gyr}$, even though the deviation between the frozen potential and the living potential orbits can be large for the backsplash solutions, e.g. 52 kpc for a tangential velocity of $50\,{\rm km\,s^{-1}}$, the distances between the satellite and the MW deviate only by 10 per cent or less, and the velocity deviates only by $15\,{\rm km\,s^{-1}}$ or lower. This means that, for the range of explored backsplash orbits, the dynamical friction can change the direction of the velocity and the direction of the orbit, but the magnitude of the velocity, reaching then similar large apocentre distances. We also tested how well approximated would

be the analytical orbits between the moment after the satellite passed through the MW centre and its current position. For this, we repeat the previous simulations, but now we position the *N*-body model of Leo T at $-7\,{\rm Gyr}$ instead of $-12\,{\rm Gyr}$, finding a deviation in distance for backsplash orbits of 2 per cent (Table 4).

How is the satellite affected by the tidal forces of the MW for the different orbits? As expected, the first infall orbits, with $|\vec{u}_t^{\rm GSR}| > 90\,{\rm km\,s^{-1}}$, do not experience strong tidal effects. The backsplash solutions with wide orbits and velocities between $|\vec{u}_t^{\rm GSR}| > 50$ and $80\,{\rm km\,s^{-1}}$ decrease the central stellar and dark matter densities, as shown in Fig. A4. Backsplash orbits with $|\vec{u}_t^{\rm GSR}| < 50\,{\rm km\,s^{-1}}$ produce a decrease of the central density of one to two orders of magnitude below the initial profiles. We note that even though the stellar density profile becomes shallower, the stars are still bound to the satellite, as the cumulative mass profile reveals in Fig. A4. However, an important fraction of dark matter (up to 50 per cent) can be stripped for extremely radial orbits.

None the less, if we take a more concentrated and more massive dark matter halo model for Leo T, we find that it could survive to radial orbits with tangential velocities as low as $20\,{\rm km\,s^{-1}}$. In Fig. A4, we show the density profiles of a dwarf model with the NFW dark matter profile. As this profile has a cuspy density and a more massive dark matter halo, the tidal disruption is much weaker and the density in the central few hundred parsec is only perturbed for more radial orbits with $|\vec{u}_t^{\rm GSR}| < 20\,{\rm km\,s^{-1}}$. This is not surprising as known from several studies (Penarrubia, Navarro & McConnachie 2008; van den Bosch et al. 2017). Furthermore, we note here that, while a progenitor for this dwarf galaxy could be found, using methods developed in Fellhauer et al. (2008), Blana et al. (2015), and Matus Carillo et al. (2019) (see also Dominguez et al. 2016), this is beyond the scope of this study. The purpose of our numerical experiment here is to show that a satellite on such backsplash orbits could survive a tidal disruption by the MW, and even provide a mechanism to generate a core in the central dark matter distribution.

4.4 Satellites in the outer rim of the MW halo

We also applied our method to find first infall and backsplash orbits to a selection of distant dwarfs located beyond the virial radius of the MW (288 kpc): Cetus, Eridanus II, and Phoenix I. We explored eight different directions of the tangential velocity $\vec{u}_t^{\rm GSR}$ (every $\Delta\rm PA = 45°$), and 70 values of $|\vec{u}_t^{\rm GSR}|$, between 0 and $350\,{\rm km\,s^{-1}}$ (with a higher sampling within $30\,{\rm km\,s^{-1}}$), exploring in total a velocity grid with 560 values.

Cetus and Eridanus II have no cold gas (only an upper limit H I detectable threshold). In the scenario that these satellites lost their gas due to ram-pressure stripping, how could we estimate the satellite's pre-existing cold gas, its density, and its thermal pressure before it lost its gas? We can use the H I size–mass relation (Begum et al. 2008; Wang et al. 2016), which is observed for galaxies covering a wide range of H I masses, from Leo T, to the Magellanic Clouds, the MW, M31, and more massive galaxies (see fig. 1 in Wang et al. 2016), with their parameters for the relation:

$$\log\left(\frac{2\,R_{\rm H\,I}}{[\,{\rm kpc}]}\right) = (0.506 \pm 0.003)\log\left(\frac{M_{\rm H\,I}}{[\,{\rm M_\odot}]}\right) - (3.293 \pm 0.009).$$

(8)

The H I-size relation implies a roughly constant surface gas density (or column density) $\Sigma_{\rm H I} \approx \Sigma_{\rm o}$. If we take a constant density core, it would relate the central gas density and its scale length in the form: $\Sigma_{\rm o} \propto M_{\rm H I} r_{\rm H I}^{-2} \propto \rho_{\rm H I} \times r_{\rm H I}$. Furthermore, Stevens et al. (2019) find that the H I-size relation would be robust to ram-pressure stripping

Table 5. Orbital constraints for Cetus.

Threshold: Case	$\langle|\vec{u}_{\text{tBAS}}^{\text{GSR}}|\rangle$ km s^{-1}	$\langle D_{\min}^{\text{BAS}}\rangle$ kpc	$\langle|\vec{u}_{\text{tRPS}}^{\text{GSR}}|\rangle$ km s^{-1}	$\langle D_{\min}^{\text{RPS}}\rangle$ kpc
3	54^{+2}_{-5}	287	22^{+1}_{-8}	55^{+1}_{-12}
3a	39^{+2}_{-3}	263	19^{+1}_{-7}	54^{+1}_{-12}
3b	66^{+2}_{-7}	308	24^{+1}_{-8}	56^{+1}_{-12}
4	31^{+1}_{-3}	184^{+5}_{-3}	13^{+1}_{-5}	50^{+0}_{-7}
4a	11^{+1}_{-1}	164^{+2}_{-2}	$(^a)$	$(^a)$
4b	43^{+2}_{-4}	229^{+9}_{-4}	16^{+1}_{-6}	53^{+1}_{-9}
cos4	42^{+2}_{-5}	290^{+2}_{-2}	16^{+2}_{-7}	64^{+2}_{-15}
B.V.($\pm\Delta$)	31^{+37}_{-21}	184^{+124}_{-19}	13^{+13}_{-13}	50^{+71}_{-9}

Note. (^{a}) There are no values for case 4a for Cetus that can produce ram-pressure-stripped orbits, as can be seen in Fig. A5.

Table 6. Orbital constraints for Eridanus II.

Threshold: Case	$\langle|\vec{u}_{\text{tBAS}}^{\text{GSR}}|\rangle$ km s^{-1}	$\langle D_{\min}^{\text{BAS}}\rangle$ kpc	$\langle|\vec{u}_{\text{tRPS}}^{\text{GSR}}|\rangle$ km s^{-1}	$\langle D_{\min}^{\text{RPS}}\rangle$ kpc
3	94^{+6}_{-11}	287	31^{+27}_{-17}	38^{+20}_{-10}
3a	64^{+9}_{-10}	263	23^{+32}_{-15}	35^{+21}_{-7}
3b	117^{+5}_{-10}	308	37^{+24}_{-18}	40^{+19}_{-12}
4	70^{+9}_{-10}	211^{+3}_{-12}	24^{+23}_{-14}	40^{+17}_{-9}
4a	39^{+11}_{-10}	166^{+1}_{-3}	9^{+27}_{-9}	36^{+14}_{-6}
4b	93^{+6}_{-11}	257^{+6}_{-16}	31^{+21}_{-16}	41^{+16}_{-11}
cos4	76^{+7}_{-10}	284^{+1}_{-2}	23^{+20}_{-13}	42^{+18}_{-9}
B.V.($\pm\Delta$)	70^{+51}_{-41}	211^{+97}_{-48}	24^{+37}_{-24}	40^{+20}_{-12}

Notes. B.V. are the best values selected from case 4 with the errors estimated as in Table 3.

as well. As we find that in Leo T the H I radius (R_{HI}) is similar to the stellar half-light radius R_{Pl}^{V} to within 4 per cent difference, we use the stellar half-light radius of these satellites as a proxy for their R_{HI} values to estimate the H I mass that they would have contained. Then, assuming a Plummer profile, we estimate a central density and an H I-mass-to-stellar light ratio for Cetus and Eridanus II of 1.5 and 17 $M_\odot\,L_\odot^{-1}$, respectively. These assumptions, while arbitrary, would locate these pairs on the gas-rich side of what is observed for other distant gas-rich dwarfs of the LG (McConnachie 2012; Spekkens et al. 2014). We test these results using the values of the central gas density and H I mass of Leo T for these dwarfs, also finding ram-pressure-stripped orbits with similar values for the tangential velocities.

We present our findings below, and the main properties of the explored orbits in Tables 5 and 6 and in Fig. A5:

(i) *Cetus*: This dwarf is located at $D_\odot = 755 \pm 24$ kpc or $\sim 2.6 R_{\text{vir}}$ from the MW (McConnachie & Irwin 2006), with an LOS GSR stellar velocity of $v_{\text{los},\star}^{\text{GSR}} = -14.85 \pm 1.7$ km s^{-1} (Taibi et al. 2018). Its absolute magnitude is $M_{\text{V}} = -11.3 \pm 0.3$ mag (McConnachie & Irwin 2006), and its stellar mass is $5.9 \times 10^6\,M_\odot$, which is ~ 30 times larger than that in Leo T. Its stellar velocity dispersion implies a dynamical mass of $M_{\text{r3Dh}}^{\text{dyn}} = 67^{+19}_{-16} \times 10^6\,M_\odot$ (Taibi et al. 2018) within its 3D-half-light radius ($r_{\text{3Dh}} \approx 4/3 R_{\text{Pl}} = 791 \pm 29$ pc) (McConnachie & Irwin 2006).

Taibi et al. (2018) hypothesize that, given that Cetus has no detectable H I (Spekkens et al. 2014), it could be a backsplash system that lost all its gas during a passage through the MW. In Fig. A5, we show that surprisingly there is indeed a range of tangential velocities that result

in backsplash solutions for Cetus, when $|\vec{u}_{\text{tBAS}}^{\text{GSR}}| \leq 31^{+37}_{-21}$ km s^{-1} (or see as proper motions in Fig. 11), which for case 4 happened at a range of $t\left(D_{\min}^{\text{BAS}}\right) = -11.9 \pm 0.1$ Gyr while with the cosmic expansion for case cos4 was at $t\left(D_{\min}^{\text{BAS}}\right) = -7.4 \pm 0.1$ Gyr.

While several mechanisms to remove the cold gas in field dwarfs are possible, such as UV background evaporation as shown in the NIHAO simulations (Buck et al. 2019), it is very interesting that we indeed find a range of ram-pressure-stripped backsplash orbits for $|\vec{u}_{\text{tRPS}}^{\text{GSR}}| \leq 13^{+12}_{-13}$ km s^{-1} (Fig. 11), which for case 4 happened at a range of $t\left(D_{\min}^{\text{RPS,2}}\right) = -11.1^{+0.2}_{-0.1}$ Gyr while for case cos4 was at $t\left(D_{\min}^{\text{RPS,2}}\right) = -6.6^{+0.1}_{-0.1}$ Gyr, and for case 3 we find $t\left(D_{\min}^{\text{RPS,2}}\right) = -10.2^{+0.3}_{-0.1}$ Gyr. The exception where we find no ram-pressure solutions is the extreme case 4a, where Cetus is too far and the time-depending MW virial mass is too small at high redshift to have brought the dwarf close enough to strip its gas (see Table 5). Of course, given that Cetus is far, we would expect the whole MW region attracting the satellite, a scenario better represented by case 1 or 3. The maximum and minimum limits of the velocity thresholds are given by largest and smallest variations between cases, which are driven mostly by virial mass of the MW, of case 3b and case 4a, respectively.

We note that no GSR tangential velocity ($|\vec{u}_{\text{t}}^{\text{GSR}}| = 0$ km s^{-1}) would result in the proper motions of $\mu_{\alpha*}^\circ = 0.037$ mas yr^{-1} and $\mu_\delta^\circ = -0.056$ mas yr^{-1}.

Given that Cetus currently is closer to M31 than to the MW, and that it presents no evidence for a stellar truncation radius, McConnachie & Irwin (2006) argue that this dwarf might have always been in isolation in the past. Here we report that we find no orbits passing near M31 in the past for this dwarf within the considered range of parameters.

(ii) *Eridanus II*: It is located at $D_\odot = 366 \pm 17$ kpc from the MW $\sim 1.27 R_{\text{vir}}$ (Crnojević et al. 2016; Li et al. 2017), with an LOS GSR stellar velocity of $v_{\text{los},\star}^{\text{GSR}} = -76.8 \pm 2.0$ km s^{-1} (Li et al. 2017).[3] It has a luminosity of $L_{\text{V}} = 5.9^{+1.9}_{-1.4} \times 10^4\,L_\odot$ with a 3D half-light radius of $r_{\text{3D-half}} = 369 \pm 18$ pc and a dynamical mass within this of $M_{\text{r3Dh}}^{\text{dyn}} = 12^{+4}_{-3} \times 10^6\,M_\odot$ (Li et al. 2017). We also find a range of backsplash solutions for $|\vec{u}_{\text{t}}^{\text{GSR}}| \leq 68^{+53}_{-39}$ km s^{-1} (see Fig. A5 and Table 6), which for case 4 happened at a range of $t\left(D_{\min}^{\text{BAS}}\right) = -11.7 \pm 0.3$ Gyr, while including the cosmic expansion was at $t\left(D_{\min}^{\text{BAS}}\right) = -6.8^{+1.2}_{-2.3}$ Gyr. We also find a range of ram-pressure-stripped backsplash solutions for $|\vec{u}_{\text{t}}^{\text{GSR}}| \leq 16^{+38}_{-16}$ km s^{-1}. Particularly, for case 4 the treshold for ram pressure stripped orbits happened at $t\left(D_{\min}^{\text{RPS,2}}\right) = -7.7^{+0.2}_{-0.6}$ Gyr while for case cos4 was at $t\left(D_{\min}^{\text{RPS,2}}\right) = -5.4^{+0.1}_{-0.3}$ Gyr, and for case 3 we find $t\left(D_{\min}^{\text{RPS,2}}\right) = -7.2^{+0.3}_{-0.8}$ Gyr.

Fritz et al. (2018) estimate proper motions for several Milky Way satellites from Gaia DR2, finding for Eridanus II $\mu_{\alpha*} = 0.159 \pm 0.292 \pm 0.053$ mas yr^{-1} and $\mu_\delta = 0.372 \pm 0.340 \pm 0.053$ mas yr^{-1} (statistical and systematic errors). Recent estimates from McConnachie & Venn (2020)[4] find similar proper motion values. We find that these values and their error range overlap with our region of first in-fall solutions, as well as with our backsplash region (Fig. 11). However, the gas stripped backsplash region does not overlap with the observations under the assumed gas density core. We note that a $|\vec{u}_{\text{t}}^{\text{GSR}}| = 0$ km s^{-1} translates into $\mu_{\alpha*}^\circ = 0.094$ mas yr^{-1} and $\mu_\delta^\circ = -0.062$ mas yr^{-1} for this satellite.

(iii) *Phoenix I*: This dwarf is similar to Leo T in terms of mass and distance. It is located at $D_\odot = 409 \pm 23$ kpc ($\sim 1.4 R_{\text{vir}}$) from the MW

---

[3]Recomputed for the Galactic frame used here.
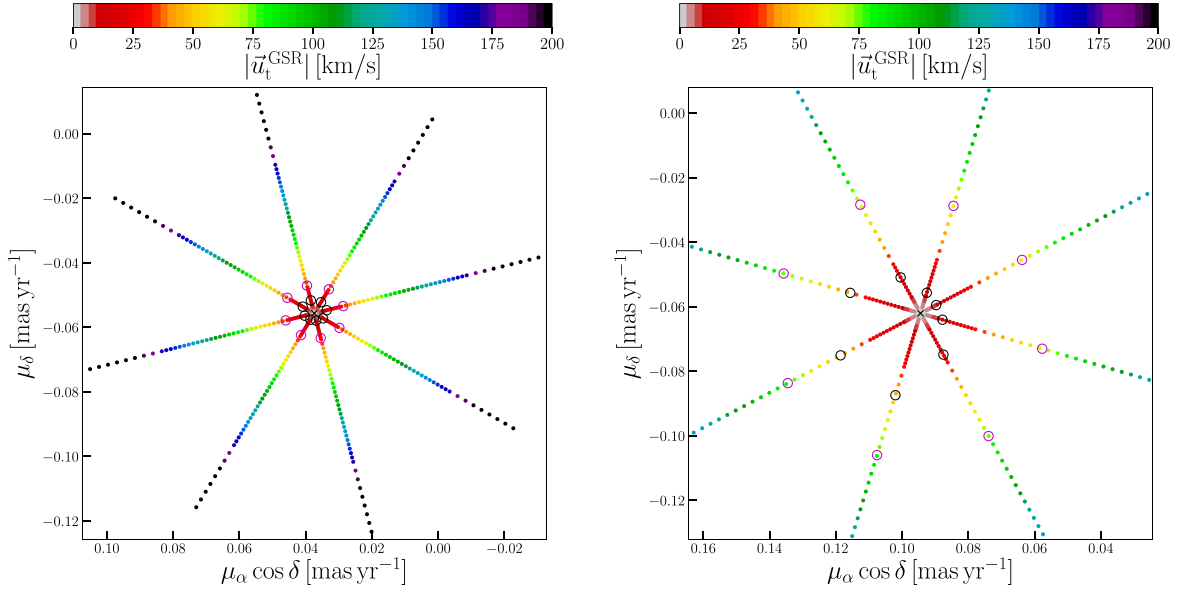[4]We note that the authors have updated their values.

Figure 11. Proper motions explored for Cetus (left-hand panel) and Eridanus II (right-hand panel) at their current positions for case 4 as a function of $|\vec{u}_t^{GSR}|$ (colour bar). Each radial set of points corresponds to different directions of $\vec{u}_t^{GSR}$. The black small circles surrounding the centre mark the ram-pressure-stripped region due to $P_{R,2}$, and the magenta circles mark the backsplash solution region.

(Battaglia et al. 2012) [previous estimates are $D_\odot = 415 \pm 19$ kpc (McConnachie et al. 2005) and 420 ± 10 kpc (Young et al. 2007)]. Its projected half-light radius is $R_h^V = 2.3 \pm 0.07$ arcmin (274 $\pm$ 8 pc) (Battaglia et al. 2012) and luminosity is $L_V = 7.6 \times 10^5$ L$_\odot$ (re-scaled to a distance of 409 kpc). Kacharov et al. (2017) report a stellar velocity dispersion of $\sigma_{los,\star} = 9.2 \pm 0.7$ km s^{-1}. We assume a constant dispersion profile, and we use the virial relation (5) to find a dynamical mass of $M_{half}^{dyn} = 2.1 \pm 0.3 \times 10^7$ M$_\odot$ within the half-light radius and a mass-to-light ratio of $M/L_V = 56$ M$_\odot$ L$_\odot^{-1}$.

Intriguingly, Phoenix also has an H I cloud that is offset from the stellar centre, with larger separation, however, of about 300 arcsec (595 pc), with the H I distribution not only showing a different systemic velocity from the stellar one, but it also shows a velocity gradient (St-Germain et al. 1999). Young et al. (2007) determine an H I mass of 1.1×10^5 M$_\odot$ and a central surface density of 0.512×10^{20} cm^{-2} (or 0.55 M$_\odot$ kpc^{-2}, including He), where we have re-scaled it to a distance of 409 kpc. Assuming that the central density follows a Plummer profile, we find a gas core density and scale of $\rho_{Pl}^{gas} = 1.4 \times 10^6$ M$_\odot$ kpc^{-3} and $R_{Pl}^{gas} = 150$ arcsec (297 pc), respectively.

To calculate the orbits, we use the stellar LOS systemic velocity determined in Kacharov et al. (2017) with $v_{los,\star}^\odot = -21.2 \pm 1.0$ km s^{-1} that transforms to $v_{los,\star}^{GSR} = -116.8$ km s^{-1}, almost doubling the stellar LOS velocity of Leo T. Exploring different magnitudes and directions of tangential velocities ($\vec{u}_t^{GSR}$), we find almost exclusively first infall solutions. Only in cases 3b and in case cos4, we find some backsplash solutions when the tangential velocity is lower than 30 ± 10 km s^{-1}. This occurs because these cases are extreme scenarios with the most massive MW haloes. Even for those cases, the minimum distance that these orbits reach is half or 30 per cent of the virial radius of the MW. Furthermore, only in case cos4 we find some ram-pressure-stripped orbits for tangential velocities of 15 ± 5 km s^{-1}. Therefore, we exclude backsplash orbits for Phoenix I, making this dwarf a first infall satellite candidate.

Fritz et al. (2018) also estimate the proper motion for Phoenix I, finding $\mu_{\alpha*} = 0.079 \pm 0.099 \pm 0.04$ mas yr^{-1} and $\mu_\delta = -0.049 \pm$

0.12 ± 0.04 mas yr^{-1}, which when converted to the GSR frame is $|\vec{u}_t^{GSR}| = 68_{-66}^{+406}$ km s^{-1}. We note here that $|\vec{u}_t^{GSR}| = 0$ km s^{-1} is equivalent to $\mu_{\alpha*}^\circ = 0.083$ mas yr^{-1} and $\mu_\delta^\circ = -0.084$ mas yr^{-1}. We calculate the maximum ram pressure that the measured proper motion would imply. The thermal pressure is 7.0×10^8 M$_\odot$ kpc^{-3} km^2 s^{-2}, while the ram pressure is $1.6_{-0.4}^{+19.1} \times 10^6$ M$_\odot$ kpc^{-3} km^2 s^{-2} where the upper and lower errors come from the velocity error range. Therefore, as the ratio is always lower than one, the ram pressure would be too weak to remove its gas at its current position. McConnachie & Venn (2020) estimate new proper motions for Phoenix obtaining similar values to Fritz et al. (2018), from which we reach the same conclusion for Phoenix, that this is a field dwarf on its first in-fall.

5 SUMMARY AND CONCLUSION

Leo T's interesting properties, such as a recent star formation episode, its location at a large distance from the MW, its gas, and dark matter content, make it an excellent laboratory to study the formation and evolution of galaxies in the most idealized scenario. In this paper, we present a method to explore a wide range of orbits for the dwarf Leo T to determine if this dwarf could be a backsplash satellite, i.e. a dwarf that already passed through the MW in the past, or if it is approaching the MW for the first time.

For this purpose, we developed the code DELOREAN to explore a large number of proper motions and to calculate semi-analytical orbits backwards in time considering a number of scenarios for the gravitational potentials that include an accreting MW halo, the potential of M31, dynamical friction, and the cosmic expansion of the Universe.

Our main results are the following:

(1) We find backsplash orbital solutions for Leo T when the tangential velocity in the GSR is lower than $|\vec{u}_t^{GSR}| \leq 63_{-39}^{+47}$ km s^{-1}. We find that backsplash solutions with $|\vec{u}_t^{GSR}| > 21_{-21}^{+33}$ km s^{-1} would allow the satellite to survive the ram-pressure stripping of the MW. This suggests that Leo T could be on a backsplash orbit,

but in a wide orbit that could have reached a minimum distance of $D_{\min} \geq 38^{+26}_{-16}$ kpc in the past that allowed it to keep its gas. Therefore, Leo T could be first infall satellite or also a wide-orbit backsplash dwarf with a moderate interaction with the MW in the past. The velocity uncertainty range is dominated at first order by the uncertainty in the virial mass of the MW, where we explored a 20 per cent virial mass variations, followed by the uncertainties in the MW mass accretion history.

(2) When comparing with the H I morphology of Leo T (Adams & Oosterloo [2018]), we can select the orbits that better align with the observed H I-stellar offset, the H I inner flattening, or the H I tail, obtaining a backsplash velocity threshold of $|\vec{u}_t^{\mathrm{GSR}}| \leq 69 \pm 39$ km s^{-1}. This corresponds to a range of proper motions for different orbital solutions:

(a) first infall: $\mu_\delta < -0.1507 [\mathrm{mas\ yr^{-1}}]$;
(b) unstripped gas backsplash: $-0.1507 \leq \mu_\delta/[\mathrm{mas\ yr^{-1}}] \leq -0.1318$;
(c) gas stripped backsplash: $-0.1318 \leq \mu_\delta/[\mathrm{mas\ yr^{-1}}] \leq -0.1153$.

In Fig. 8, we provide proper motion constraints for all directions, and in Table 3 we include error ranges for different cases. A comparison with full hydrodynamical simulations that reproduce the H I features will better constrain the proper motion and evolution of Leo T (future publication). We note that new proper motion estimates for Leo T were recently published by McConnachie & Venn ([2020])[5]. We find that within the observational errors both orbital solutions can be considered.

(3) We also calculate orbits backwards in time with a cosmological scheme where space changes according to a cosmology with parameters from the Planck Collaboration XIII ([2015]). We find that the backsplash orbital solutions explored for Leo T experience a delay on their first infall of $\sim$2 Gyr later than those in the non-expanding fiducial case. This results from the cosmic expansion at $z > 1$, where backsplash orbital solutions are found at larger distances from the MW at early times, which then take longer to fall, with Hubble flow contributes iingthe delay of the first infall by decelerating the infalling satellites when $H(z)$ was large.

(4) We applied our method to the distant dwarfs Cetus, Eridanus II, and Phoenix I. We find a range of backsplash solutions for Cetus where the gas ram pressure of the MW could have been large enough to strip its gas, providing an explanation for its current absence of cold gas. For Eridanus II we also find backsplash solutions that lay within the range of proper motion observational estimations (Fritz et al. [2018]; McConnachie & Venn [2020]) however, under our assumed gas density core, the they lay near but outside the ram pressure stripped orbital solutions. For Phoenix I, we find neither ram-pressure-stripped nor backsplash solutions. This is due to the large LOS velocity, suggesting that this dwarf is a pristine dwarf on its first infall. Finally, we also use our cosmological orbital calculation for these dwarfs, where we also find a time delay of the first pericentre passage in the backsplash solutions of $\Delta t \approx 2$ Gyr for Eridanus II and of $\Delta t \approx 5$ Gyr for Cetus.

We conclude that, while the H I-rich dwarf Leo T could be a backsplash system with some mild interaction with the MW in the past, Phoenix I is likely a pristine system, and therefore, both the systems are interesting laboratories to test formation and evolution models of dwarf galaxies in isolation or interaction regimes. Certainly, cosmological galaxy simulations predict that 30–50 per cent

of the satellites between one and two times the virial radius of host galaxies like the MW or Andromeda are a backsplash population, while the remaining are first infall dwarfs. This raises up great expectations that, with the upcoming telescopes, such as the Vera C. Rubin Observatory,[6] we will discover many more distant dwarf satellites, including backsplash population members.

DATA AVAILABILITY

Data available on request.[7]

REFERENCES

Adams E. A. K., Oosterloo T. A., 2018, A&A, 612, 12 (AO18)
Battaglia G. et al., 2012, MNRAS, 424, 1113
Begum A., Chengalur J. N., Karachentsev I. D., Sharina M. E., Kaisin S. S., 2008, MNRAS, 386, 1667
Belokurov V., Erkal D., Deason A. J., Koposov S. E., De Angeli F., Evans D. W., Fraternali F., Mackey D., 2017, MNRAS, 466, 4711
Belokurov V. et al., 2018, MNRAS, 478, 611
Binney J., Tremaine S., 2008, Phys. Today, 62, 56
Blana M., Fellhauer M., Smith R., Candlish G. N., Cohen R., Farias J. P., 2015, MNRAS, 446, 144
Bland-Hawthorn J., Gerhard O., 2016, ARA&A, 54, 529 (BG16)
Blitz L., Robishaw T., 2000, ApJ, 541, 675
Bond J. R., Cole S., Efstathiou G., Kaiser N., 1991, ApJ, 379, 440
Bovy J., 2015, ApJS, 216, 29
Bovy J., Rix H.-W., 2013, ApJ, 779, 30
Broeils A. H., Rhee M. H., 1997, A&A, 324, 877
Buck T., Macciò A. V., Dutton A. A., Obreja A., Frings J., 2019, MNRAS, 483, 1314
Burkert A., 1995, ApJ, 447, L25
Burkert A., 2015, ApJ, 808, 10
Clementini G., Cignoni M., Ramos R. C., Federici L., Ripepi V., Marconi M., Tosi M., Musella I., 2012, ApJ, 756, 108
Correa C. A., Stuart J., Wyithe B., Schaye J., Duffy A. R., 2015c, MNRAS, 452, 1217

[5]We note that the authors have updated their values.

[6]https://www.lsst.org
[7]http://matiasblana.github.io

Correa C. A., Wyithe J. S. B., Schaye J., Duffy A. R., 2015a, MNRAS, 450, 1514

Correa C. A., Wyithe J. S. B., Schaye J., Duffy A. R., 2015b, MNRAS, 450, 1521

Courteau S., van den Bergh S., 1999, AJ, 118, 337

Crnojević D., Sand D. J., Zaritsky D., Spekkens K., Willman B., Hargis J. R., 2016, ApJ, 824, 6

Deason A. J., Belokurov V., Koposov S. E., Lancaster L., 2018, ApJ, 862, L1

Deason A. J., Fattahi A., Frenk C. S., Grand R. J. J., Oman K. A., Garrison-Kimmel S., Simpson C. M., Navarro J. F., 2020, MNRAS, 496, 3929

Dehnen W., 2000, ApJS, 536, L39

de Jong J. T. A. et al., 2008, ApJ, 680, 1112

Diemer B., 2020, preprint (arXiv:2007.10992)

Diemer B. et al., 2017a, https://iopscience.iop.org/article/10.3847/1538-4365/aa799c

Diemer B. et al., 2017b, https://iopscience.iop.org/article/10.3847/1538-4357/aa79ab

Dominguez R., Fellhauer M., Blaña M., Farias J.-P., Dabringhausen J., Candlish G. N., Smith R., Choque N., 2016, MNRAS, 461, 3630

Faerman Y., Sternberg A., McKee C. F., 2013, ApJ, 777, 14

Fellhauer M., Wilkinson M. I., Evans N. W., Belokurov V., Irwin M. J., Gilmore G., Zucker D. B., Kleyna J. T., 2008, MNRAS, 385, 1095

Fellhauer M. et al., 2006, ApJ, 651, 167

Fritz T. K., Battaglia G., Pawlowski M. S., Kallivayalil N., van der Marel R., Sohn T. S., Brook C., Besla G., 2018, A&A, 619, A103

Garrison-Kimmel S. et al., 2017, MNRAS, 471, 1709

Gatto A., Fraternali F., Read J. I., Marinacci F., Lux H., Walch S., 2013, MNRAS, 433, 2749

Gill S. P. D., Knebe A., Gibson B. K., Gill S. P. D., Knebe A., Gibson B. K., 2005, MNRAS, 356, 1327

Grcevich J., Putman M. E., 2009, ApJ, 696, 385

Haggar R., Gray M. E., Pearce F. R., Knebe A., Cui W., Mostoghiu R., Yepes G., 2020, MNRAS, 492, 6074

Hausammann L., Revaz Y., Jablonka P., 2019, A&A, 624, A11

Haywood M., Di Matteo P., Lehnert M. D., Snaith O., Khoperskov S., Gómez A., 2018, ApJ, 863, 113

Helmi A. et al., 2018, Nature, 563, 85

Irwin M. J. et al., 2007, ApJ, 656, L13

Jedrzejewski R. I., 1987, MNRAS, 226, 747

Kacharov N. et al., 2017, MNRAS, 466, 2006

Kalberla P. M., Kerp J., 2009, ARA&A, 47, 27

Kam S. Z., Carignan C., Chemin L., Foster T., Elson E., Jarrett T. H., 2017, AJ, 154, 41

Karachentsev I. D., Kashibadze O. G., Makarov D. I., Tully R. B., 2009, MNRAS, 393, 1265

Li T. S. et al., 2017, ApJ, 838, 15

Li Y.-S., White S. D. M., 2008, MNRAS, 384, 1459

Lotz M. et al., 2019, MNRAS, 488, 5370

Matus Carillo D. R., Fellhauer M., Alarcon Jara A. G., Aravena C. A., Urrutia Zapata F., 2020, A&A, 633, 10

McConnachie A., Irwin M., 2006, MNRAS, 365, 1263

McConnachie A. W., 2012, AJ, 144, 36

McConnachie A. W., Irwin M. J., Ferguson A. M. N., Ibata R. A., Lewis G. F., Tanvir N., 2005, MNRAS, 356, 979

McConnachie A. W., Venn K. A., 2020, preprint (arXiv:2007.05011)

Miller M. J., Bregman J. N., 2015, ApJ, 800, 19

Mo H., van den Bosch F. C., White S., 2010, in Mo H., van den Bosch F., White S., eds, Galaxy Formation and Evolution. Cambridge Univ. Press, Cambridge, UK

Mori M., Burkert A., 2000, ApJ, 538, 559

Niederste-Ostholt M., Belokurov V., Evans N. W., Penarrubia J., Niederste-Ostholt M., Belokurov V., Evans N. W., Peñarrubia J., 2010, ApJ, 712, 516

Nulsen P. E. J., 1982, MNRAS, 198, 1007

Ogiya G., Mori M., Ishiyama T., Burkert A., 2014, MNRAS, 440, L71

Patra N. N., 2018, MNRAS, 480, 4369

Penarrubia J., Navarro J. F., McConnachie A. W., 2008, ApJ, 673, 226

Perret V., 2016, Astrophysics Source Code Library, record ascl:1607.002

Perret V., Renaud F., Epinat B., Amram P., Bournaud F., Contini T., Teyssier R., Lambert J. C., 2014, A&A, 562, 39

Peñarrubia J., Ma Y.-Z., Walker M. G., McConnachie A., 2014, MNRAS, 443, 2204

Planck Collaboration XIII, 2015, A&A, 594, A13

Press W. H., Schechter P., 1974, ApJ, 187, 425

Quinn T., Katz N., Stadel J., Lake G., 1997, preprint (astro-ph/9710043)

Read J. I., Agertz O., Collins M. L. M., 2016, MNRAS, 459, 2573

Rodriguez Wimberly M. K., Cooper M. C., Fillingham S. P., Boylan-Kolchin M., Bullock J. S., Garrison-Kimmel S., 2019, MNRAS, 483, 4031

Ruiz-Lara T., Gallart C., Bernard E. J., Cassisi S., 2020, Nat. Astron.

Ryan-Weber E. V., Begum A., Oosterloo T., Pal S., Irwin M. J., Belokurov V., Evans N. W., Zucker D. B., 2008, MNRAS, 384, 535

Salem M., Besla G., Bryan G., Putman M., van der Marel R. P., Tonnesen S., 2015, ApJ, 815, 77

Sawala T., Scannapieco C., White S., 2012, MNRAS, 420, 1714

Simon J. D., Geha M., 2007, ApJ, 670, 313

Simpson C. M., Grand R. J. J., Gómez F. A., Marinacci F., Pakmor R., Springel V., Campbell D. J. R., Frenk C. S., 2018, MNRAS, 478, 548

Spekkens K., Urbancic N., Mason B. S., Willman B., Aguirre J. E., 2014, ApJ, 795, L5

Springel V., Di Matteo T., Hernquist L., 2005, MNRAS, 361, 776

St-Germain J., Carignan C., Côte S., Oosterloo T., 1999, AJ, 118, 1235

Stevens A. R. H., Diemer B., Lagos C. d. P., Nelson D., Obreschkow D., Wang J., Marinacci F., 2019, MNRAS, 490, 96

Taibi S. et al., 2018, A&A, 618, 22

Tamm A., Tempel E., Tenjes P., Tihhonova O., Tuvikene T., 2012, A&A, 546, A4

Teuben P., 1995, Astron. Data Anal. Softw. Syst. IV, 77

Teyssier M., Johnston K. V., Kuhlen M., 2012, MNRAS, 426, 1808

The Astropy Collaboration, 2013, A&A, 558, A33

The Astropy Collaboration, 2018, AJ, 156, 123

Tonnesen S., 2019, ApJ, 874, 161

van den Bosch F. C., Ogiya G., 2018, MNRAS, 475, 4066

van den Bosch F. C., Ogiya G., Hahn O., Burkert A., 2017, MNRAS, 474, 3043

van den Bosch F. C., Ogiya G., Hahn O., Burkert A., 2018, MNRAS, 474, 3043

van der Marel R. P., Besla G., Cox T. J., Sohn S. T., Anderson J., 2012, ApJ, 753, 9

van der Marel R. P., Fardal M. A., Sohn S. T., Patel E., Besla G., del Pino-Molina A., Sahlmann J., Watkins L. L., 2018, ApJ, 872, 24

Wang J., Koribalski B. S., Serra P., van der Hulst T., Roychowdhury S., Kamphuis P., Chengalur J. N., 2016, MNRAS, 460, 2143

Watkins L. L., Evans N. W., An J. H., 2010, MNRAS, 406, 264

Weisz D. R. et al., 2012, ApJ, 748, 6

Wolf J., Martinez G. D., Bullock J. S., Kaplinghat M., Geha M., Munoz R. R., Simon J. D., Avedo F. F., 2009, MNRAS, 406, 1220

Young L. M., Skillman E. D., Weisz D. R., Dolphin A. E., Young L. M., Skillman E. D., Weisz D. R., Dolphin A. E., 2007, ApJ, 659, 331

APPENDIX A: TOOLS OF DELOREAN

A1 Proper motion exploration

Our code DELOREAN has the option to calculate orbits providing directly heliocentric proper motion values pre-defined by the user. The code can also construct the vector $\vec{u}_t^{\rm GSR}$ that is tangential to the LOS velocity in the GSR frame at the current position of the object, which is basically derived from the plane of angular momentum. It starts by converting $\vec{v}_{\rm los}^{\rm GSR}$ to GC coordinates $\vec{v}_{\rm los}^{\rm GC}$. Then, it builds two orthonormal vector bases of $\vec{u}_t^{\rm GSR}$ in the GC frame, which are perpendicular to the LOS velocities $\vec{v}_{\rm los}^{\rm GC}$. For this, it uses the angular
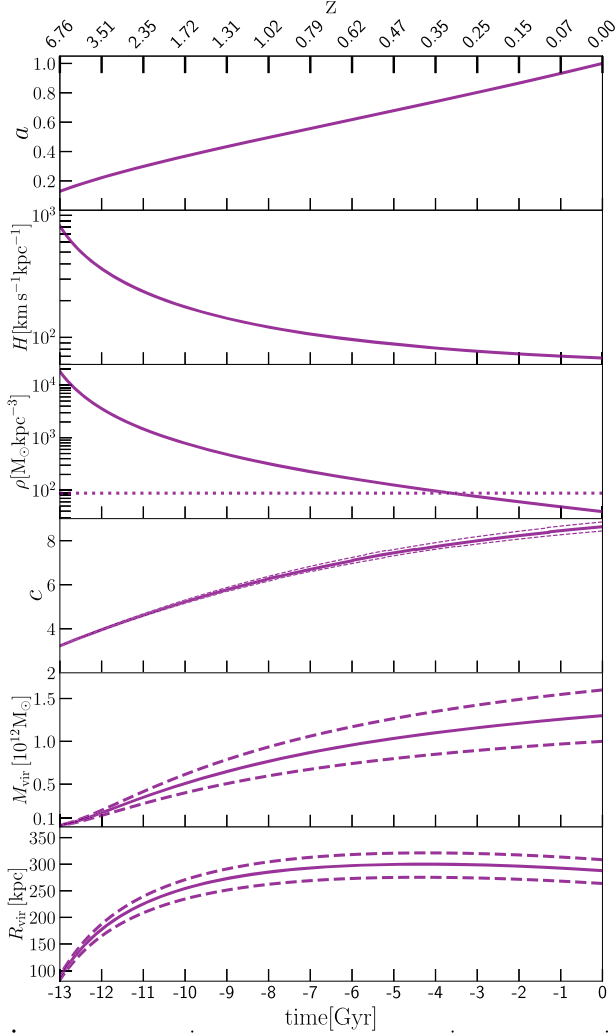
Figure A1. In the top to third panel, are shown as a function of lookback time (redshift): scale factor, expansion factor, matter density ($\rho_{\rm m} = \rho_{\rm crit}\Omega_{\rm m}$) (solid curve), and dark energy density (dotted line). The values are calculated from cosmological parameters according to the Planck Collaboration XIII (2015) (Paper XIII) taken from ASTROPY (Planck15). Third to bottom panels: halo concentration, virial mass, and comoving virial radius (equation 2) as a function of redshift according to the software COMMAH (Correa et al. 2015a, b, c), which come from semi-analytical extended Press–Schechter and halo mass accretion models fitted to cosmological simulations. The values used at redshift zero for the concentration, the virial mass, and radius are 8.6, $1.3 \times 10^{12} \, {\rm M}_\odot$, and 288 kpc (solid curve), and the upper and lower dashed curves correspond to 8.8, $1.6 \times 10^{12} \, {\rm M}_\odot$, and 308 kpc and 8.4, $1.0 \times 10^{12} \, {\rm M}_\odot$, and 264 kpc, respectively.

Figure A2. Orbits integrated 12 Gyr backwards in time for case 1 (constant MW $M_{\rm vir}$), showing a range of values of $|\vec{u}_{\rm t}^{\rm GSR}|$ with selection of orbits in the direction of PA$_{\rm offset} = 3°$ to avoid overcrowding. Top panel: distance as a function of time showing the constant virial radius (288 kpc) (black dashed line). Bottom panel: velocity as a function of time.

momentum from the known LOS velocity in the GC frame:

$$\vec{u}_{\rm t}^{\rm GC} = \lambda_1 \hat{l}_{\rm los} + \lambda_2 \frac{\hat{l}_{\rm los} \times \hat{v}_{\rm los}^{\rm GC}}{|\hat{l}_{\rm los} \times \hat{v}_{\rm los}^{\rm GC}|}, \tag{A1}$$

where $\hat{l}_{\rm los}$ is the unitarian vector of $\vec{l}_{\rm los} = \vec{D} \times \vec{v}_{\rm los}^{\rm GC}$, which is a component of the total specific orbital angular momentum: $\vec{l} = \vec{D} \times (\vec{v}_{\rm los}^{\rm GC} + \vec{u}_{\rm t}^{\rm GC})$, with $\vec{D}$ being the object's GC distance. The lambda parameters define the magnitude of $\vec{u}_{\rm t}^{\rm GC}$: $|\vec{u}_{\rm t}^{\rm GSR}| = \sqrt{\lambda_1^2 + \lambda_2^2}$, and its direction is given by the angle $\theta = \arctan(\lambda_2/\lambda_1)$, which is measured on the plane of the sky, and can be converted to the position
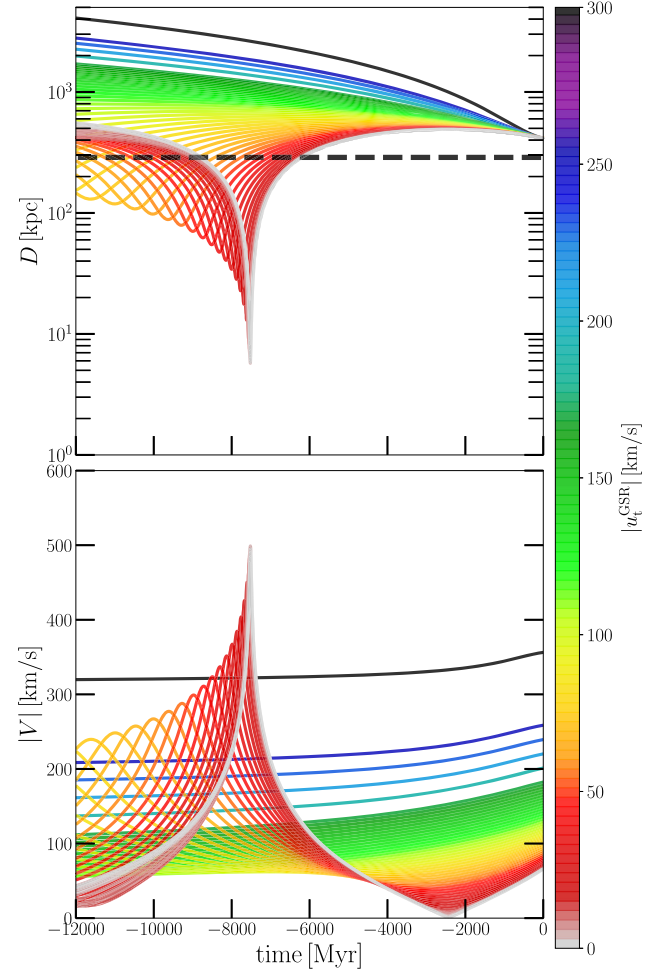
angle after conversion to equatorial coordinates (PA $= \theta - \theta_{\rm o}$). Once a value of $\vec{u}_{\rm t}^{\rm GSR}$ is defined, it can be converted into proper motions.

A2 Orbital integration with cosmic expansion

DELOREAN can also integrate orbits in a cosmological framework. For this, we pre-compute the factors in the drift (D) and kick (K) operators that depend on the cosmological parameters, using here the values from the Planck Collaboration XIII (2015) (Paper XIII) from ASTROPY (Planck15) to obtain the cosmological variables z, $a(z)$, $H(z)$, $\rho_{\rm crit}(z)$, $\rho_\Lambda(z)$, $\rho_{\rm m}(z)$, and $\Omega_{\rm m}(z)$, corresponding to the redshift, scale factor, expansion factor, critical density, matter density, dark energy density, and matter-to-critical density ratio, respectively, as functions of the lookback time (t), i.e. $z = z(t)$. We tabulate them to interpolate the values when needed (Fig. A1). These tables can be recomputed for any cosmology. To calculate the orbits, we use the symplectic form (ergo time reversible) of the equations of motion in a Hamiltonian formalism given by Quinn et al. (1997) (as applied in GADGET-2; Springel, Di Matteo & Hernquist 2005), which uses the leap-frog method, which is time reversible, to calculate the orbits in comoving coordinates ($\vec{X}$, $\vec{V}$) as
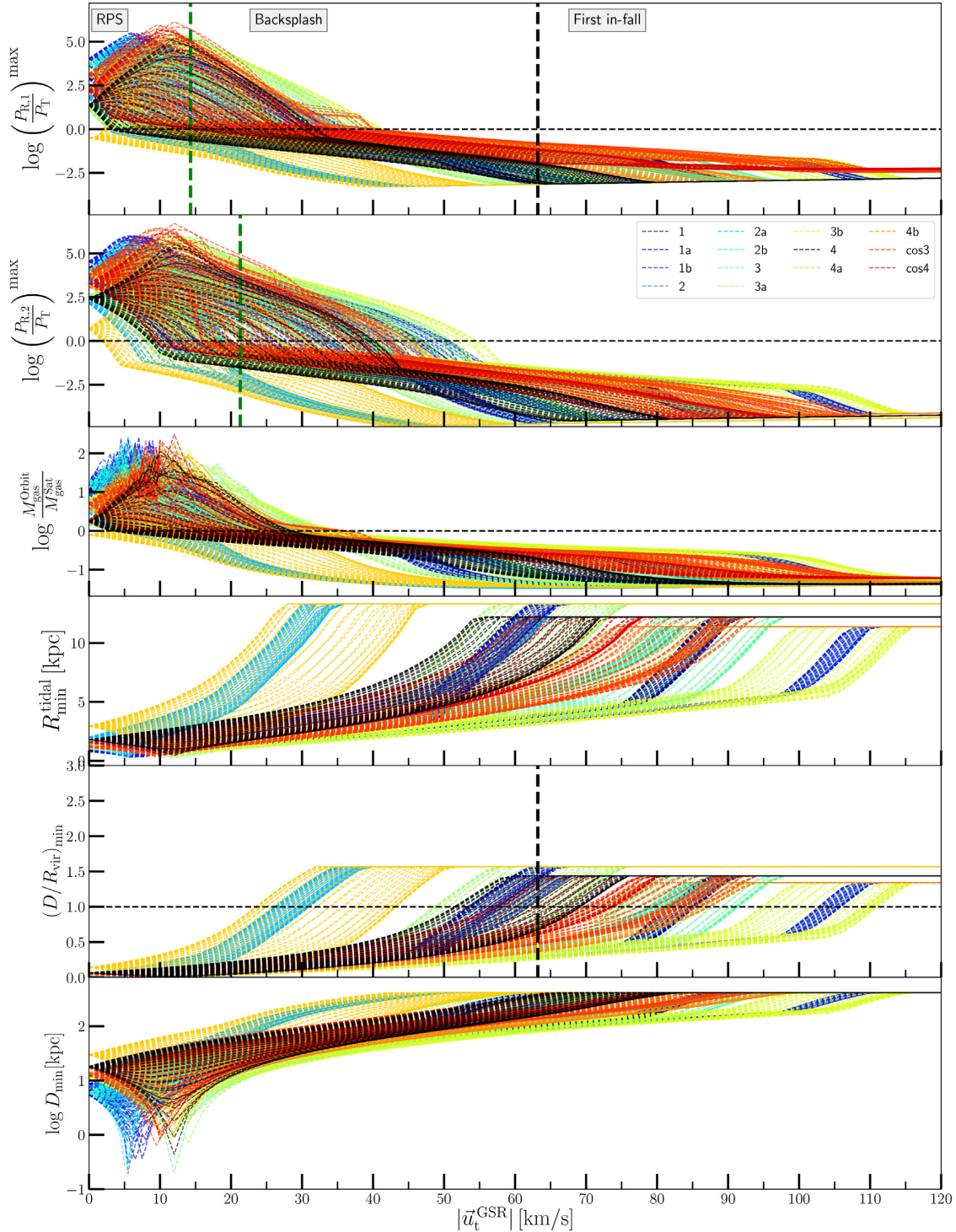
Figure A3. The main parameters for different directions of $\vec{u}_t^{GSR}$ and different cases (Table 2) as a function of $|\vec{u}_t^{GSR}|$. See the main text in Section 4.1 for the parameters' definitions. Each coloured line corresponds to a case labelled in the second top panel, where we note that our fiducial case 4 (MW accreting and M31 potential) is shown in black. From this figure, we identify three main regions in $\vec{u}_t^{GSR}$: (i) the region RPS where the MW ram pressure is larger than the thermal pressure of the satellite. Each direction and case have a slightly different value of $|\vec{u}_{tRPS}^{GSR}|$. We mark the median of P_R of our fiducial case 4 taking all directions of the tangential velocities, finding $|\vec{u}_t^{GSR}| = 14^{+26}_{-14}$ km s^{-1} for $P_{R,1}$ (top panel) and 21^{+33}_{-21} km s^{-1} for $P_{R,2}$ (second panel) (dashed green vertical lines). The error range considers the maximum and minimum threshold velocity values found among different directions of $\vec{u}_t^{GSR}$ and different cases. (ii) The backsplash region with orbits that passed through the MW dark matter halo, which we mark for case 4 at the median value and range of $|\vec{u}_t^{GSR}| = 63^{+47}_{-39}$ km s^{-1} (dashed black vertical line); and (iii) the first infall region where orbits never entered the halo.
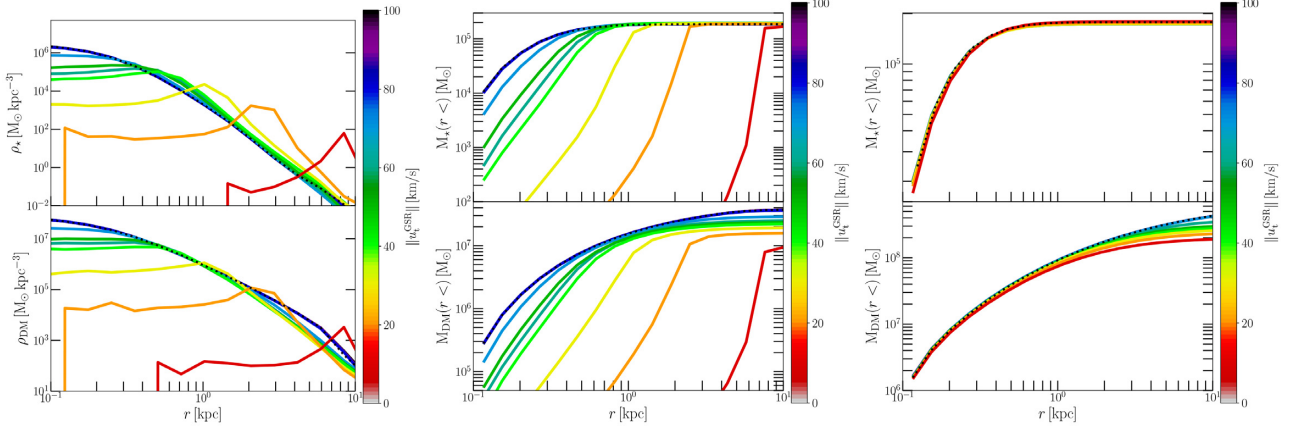
Figure A4. Left-hand panels: density profiles for model 1 showing the stellar mass profile (top subpanel) and dark matter profile (bottom subpanel) for *N*-body simulations of Leo T for different orbits. Middle panels: cumulative mass profiles of model 1 showing the stellar (top subpanel) and dark matter components (bottom subpanel) for the *N*-body models of Leo T at different snapshots. Right-hand panels: same as the middle panels but for model 2 (dwarf with a NFW dark halo). The initial profiles after the relaxation are shown with dotted curves. The coloured solid curves show the density and mass profiles of eight simulations at the final snapshot after a 12 Gyr orbit, showing the orbits with $|\vec{u}_t^{GSR}| = 30\,\mathrm{km\,s^{-1}}$ up to $100\,\mathrm{km\,s^{-1}}$.
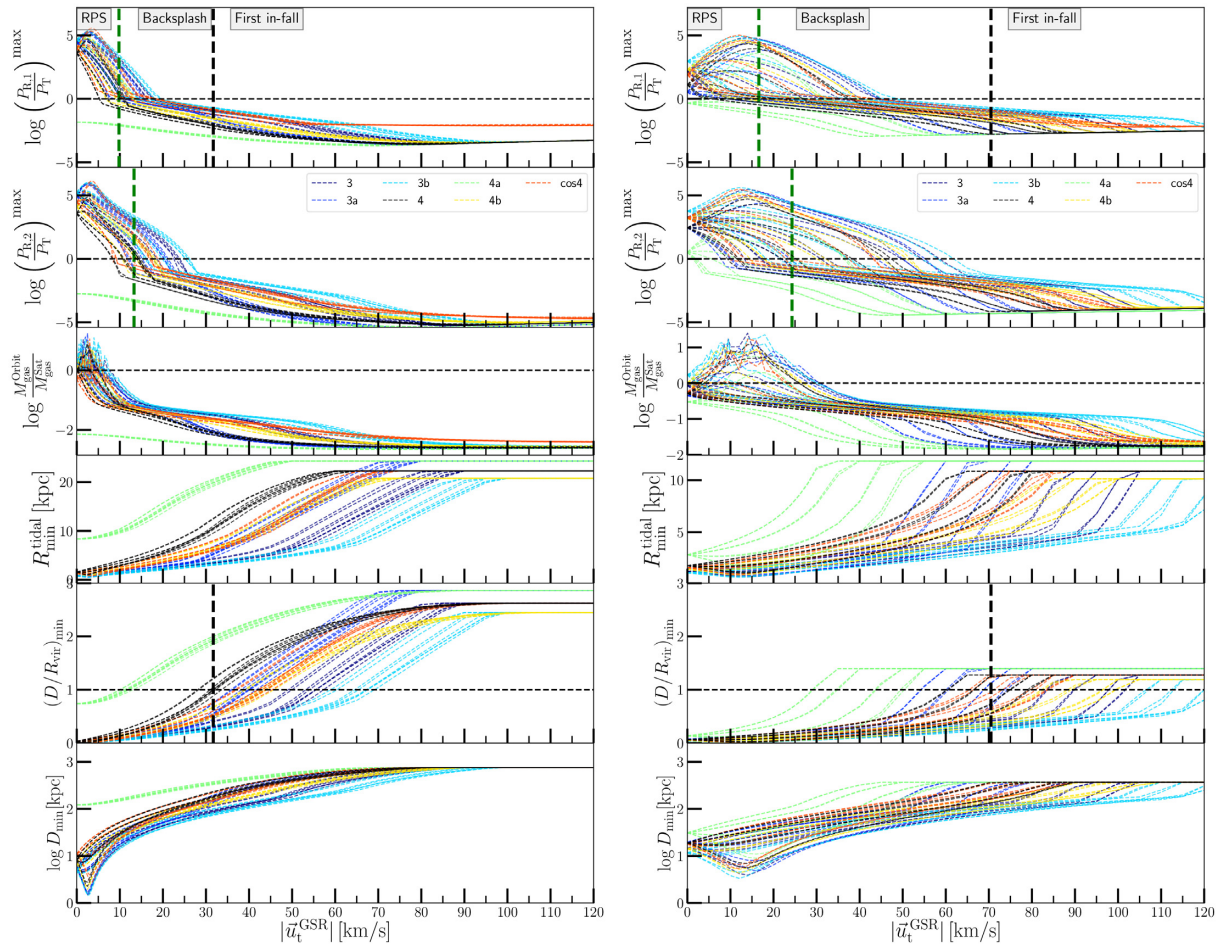

Figure A5. Main parameters explored for Cetus (left-hand panel) and Eridanus II (right-hand panel) for different directions of $\vec{u}_t^{GSR}$ orbit and different cases as a function of $|\vec{u}_t^{GSR}|$. See the main text in Section 4.1 for the parameters' definitions.

$$D\left(\Delta t\right)=\vec{X}_{t+\Delta t}=\vec{X}_t+\vec{P}\int_t^{t+\Delta t}\frac{\mathrm{d}t}{a^2}\qquad\text{(A2)}$$

$$K\left(\Delta t\right)=\vec{P}_{t+\Delta t}=\vec{P}_t-\int_t^{t+\Delta t}\mathrm{d}t\,\frac{\vec{\nabla}\psi}{a\left(t\right)},\qquad\text{(A3)}$$

where $\vec{P}=a^2\vec{V}$ is the specific canonical momentum and $\vec{\nabla}\psi$ is the gradient of the peculiar potential in comoving coordinates for the periodic boundary solution given as

$$\vec{\nabla}\psi/a=\vec{\nabla}\Phi/a-\frac{\ddot{a}}{a}a^2\vec{X},\qquad\text{(A4)}$$

with $\vec{\nabla}\Phi$ being the Newtonian gravitational potential gradient in comoving coordinates, where we used analytical potentials (i.e. disc, bulge, and dark halo), and where we use the second Friedman equation in the matter-dominated epoch to calculate the term with the second time derivative of the scale factor:

$$\frac{\ddot{a}}{a}=-\frac{4\pi G}{3}\left(\rho_\mathrm{m}-2\rho_\Lambda\right).\qquad\text{(A5)}$$

The relation between comoving $(\vec{X},\vec{V})$ and physical coordinates $(\vec{r},\vec{v})$ is given by

$$\vec{r}=a\left(t\right)\vec{X}\qquad\text{(A6)}$$

$$\vec{v}=H\left(t\right)\vec{r}+a\left(t\right)\vec{V}.\qquad\text{(A7)}$$

The peculiar velocity is then $\vec{V}_\mathrm{pec}=a\,\vec{V}$. In cases where the potential of M31 is included, the orbits of MW and M31 are pre-computed with the cosmological scheme.

This paper has been typeset from a TEX/LATEX file prepared by the author.